Title
Synthesis, Characterization and Applications of Novel Nanomaterial Systems and Semiconducting Nanowires

Permalink
https://escholarship.org/uc/item/6v41x503

Author
Martinez-Morales, Alfredo Adolfo

Publication Date
2010

Peer reviewed|Thesis/dissertation

UNIVERSITY OF CALIFORNIA
RIVERSIDE

Synthesis, Characterization and Applications of Novel Nanomaterial Systems and Semiconducting Nanowires

A Dissertation submitted in partial satisfaction
of the requirement for the degree of

Doctor in Philosophy

in

Electrical Engineering

by

Alfredo Adolfo Martinez-Morales

March 2010

Dissertation Committee:
Dr. Mihrimah Ozkan, Chairperson
Dr. Cengiz S. Ozkan
Dr. Roger Lake

The Dissertation of Alfredo Adolfo Martinez-Morales is approved:

Committee Chairperson

University of California, Riverside

Acknowledgements

My tenure at the University of California Riverside as a PhD student was filled with many unforgettable moments and life-changing opportunities. I am grateful to all of those who play a significant role (directly or indirectly) in my PhD experience.

I would like to start by thanking my advisor, Prof. Mihrimah (Mihri) Ozkan, for her constant support throughout all the phases of my PhD. Her support and guidance, allowed me to overcome many of the personal and academic challenges that are inherent to the PhD experience. I will always be thankful for the opportunity to join the Biomedical Science and Nanotechnology Laboratory (BSNL) early on in my academic career, first as an undergraduate student and later as a graduate researcher. I feel extremely fortunate for having Prof. Mihri Ozkan as my advisor. She was truly an exceptional supporter, teacher, and advisor in all the sense of the word. The exceptional quality of research being conducted in her laboratory provided me with the opportunity to publish several high impact publications and carry out important research collaborations with high caliber research groups in other universities.

I would also like to thank my co-advisor, Prof. Cengiz S. Ozkan. His insightful direction was fundamental to my research and success as a graduate student. Under his guidance, I was able to overcome many of the challenges that I encountered in my research. I am thankful for his endless words of encouragement and positive attitude.

Additionally, I would also like to thank Prof. Roger Lake, member of my defense committee and chair of the Electrical Engineering Department. His advice, support and

willingness to always accommodate my requests (including many letters of recommendation) are highly appreciated.

I also would like to thank Prof. Sheldon X.-D. Tan and Prof. Kambiz Vafai for being part of my qualifying committee.

I have a great deal of admiration and gratitude to Dr. Krishna Ver Singh, for being my research mentor when I first joined BSNL. His friendly approach and scientific insightfulness were fundamental in developing the right state of mind to successfully conduct research as an experimentalist during my PhD. His friendship was one of the highlights of my PhD experience and I will always be grateful for him openly sharing his knowledge with me.

During my PhD I was fortunate to meet and worked with many incredible individuals, particularly I would like to express my most sincere appreciation to all my labmates for the uncountable experiences (the good and the not so good) that we shared together over the years. Particularly, Dr. Sumit Chaudary and Dr. Haiwei Lu were a great source of inspiration in how to find the balance between life and research, Miroslav (Miro) Penchev was a close friend and deep collaborator with whom I had many insightful discussions about the complexities of research and life in general and Dr. Nathaniel (Nate) Portney was an excellent research collaborator and good friend with whom I hope to continue working with in the future. A huge shout out to all my labmates in the Biomedical Science and Nanotechnology Laboratory and the Biomaterials and Nanotechnology Laboratory (BNL). The financial support provided by the

Microelectronics Advanced Research Corporation (MARCO) and the Functional Engineered Nano Architectonics Focus Center (FENA) is also greatly acknowledged.

I would like to thank my wife, Jasia Martinez, for being my best friend and true love since the moment our lives crossed back in 1995. Our journey together at UC Riverside began in July 2002 as undergraduates. Since my joining to the EE PhD program in 2005, her love and kindness has healed my body and spirit from the difficulties of graduate school. She has been a great friend, loving spouse and a pillar of continuous support to do better and never give up. I am grateful for the thousands of laughs that she has brought to my life even in the most challenging of times that I experienced as PhD researcher.

I would like to thank my son, Enrique A. Martinez, for bringing an entire new perspective into my life. Although he is only 20 months old at the time of this writing, he has taught me incredible lessons about what truly matters in life and the joys of parenting. His birth has been one of the most fulfilling events during my PhD and I will always treasure his birth as one of my greatest accomplishments in my life.

I would like to thank my mother, Araceli O. Morales, for teaching me through personal example the importance of perseverance, dedication and commitment to one's work and personal dreams. Her sacrifice and unquestionable work etiquette left a long lasting impression in my own attitude towards accomplishing my professional goals.

Lastly, I would like to thank my brother, Jose (Tony) A. Martinez, whose kindheartedness, intelligence and god-loving heart have always been a source of inspiration. The maturity in his way to see life and to confront problems opened my heart, mind and senses to accept and understand the mysterious ways in which life sometimes works.

To conclude, I would like to thank with all my heart my family for all the years of unconditional love, support and always believing in me. I truly feel that I owe in great part my PhD to my family. In all true, my PhD could not be a reality, if they had not been by my side throughout this entire journey. Thank you, and this PhD is just as yours as it is mine.

To my loving wife and son

&

my mother and brother

ABSTRACT OF THE DISSERTATION

Synthesis, Characterization and Applications of Novel Nanomaterial Systems and Semiconducting Nanowires

by

Alfredo Adolfo Martinez-Morales

Doctor of Philosophy, Graduate Program in Electrical Engineering
University of California, Riverside, March 2010
Dr. Mihrimah Ozkan, Chairperson

The synthesis of novel nanomaterials systems and one-dimensioal nanostructures have created a great deal of excitement in the area of nanoelectronics and biomedical applications. The research presented in this dissertation is an effort to contribute to the realization of applications in both of the forementioned fronts of Nanotechnology.

In the first approach, a mutant icosahedral Cow Pea Mosaic Virus (CPMV) is employed as an scaffold to covalently attached two different types of inorganic nanomaterials; namely, ZnS(shell)/CdSe(core) semiconductor quantum dots and iron oxide (γ-Fe_2O_3) nanoparticles.

In the CPMV-QD(1,2) system a bistability behavior is observed and conductive atomic force microscopy (CAFM) is extensively used to characterize and implement a hybrid memory element at the nanoscale.

In the CPMV- γ-Fe_2O_3 system the conjugation of iron oxide (IO) nanoclusters is extensively characterized by magnetic force microscopy (MFM) and an increase in the local magnetic field strength opens up the potential use of this system in bioimaging applications.

On the second approach, crystalline nanowires (NWs) of semiconducting compound materials Copper Indium Disulfide ($CuInS_2$) and Indium Antimonide (InSb) are synthesized using a sono-electrochemical deposition process. Using sonoelectrochemistry overcomes many of the challenges related to the crystal quality that are inherent to regular electrochemistry and allows a greater control in the engineering of the electronic and optoelectrical properties of the as-synthesized NW

On one hand, $CuInS_2$ is a promising materials as an absorbent material for solar cell applications. During the synthesis process the effect of the partial precursor electrolyte ratios on the optoelectrical properties of the as-synthesized NWs is extensively study. As-synthesized I-rich NWs are found to be photoconductive while C-rich NWs are not.

On the other hand, InSb is an attractive material to develop high speed and low power logical applications. During the synthesis process, the depositon potential was selectively controlled as a way to modify the composition and stoichiometric ratio of the as-synthesized NWs. The transport characteristics of as-synthesized NWs were modified between n and p-type semiconducting behavior.

Table of Contents

Chapter 1 Organization and Scope of this Dissertation

Chapter 2 Memory Characterization of CPMV-QD(1,2) Hybrid System by Conductive Atomic Force Microscopy

Chapter 3 Local Magnetic Field Strength Characterization of CPMV-IO Hybrid System by Magnetic Force Microscopy

Chapter 4 Effect of electrolyte concentrations on the opto-electrical properties of sonoelectrochemically deposited Copper-Indium-Disulfide NWs

Chapter 5 Electrical Characterization of Composition Modulated $In_{1-x}Sb_x$ Nanowire Field Effect Transistors by SGM

Chapter 6 Conclusion

List of Figures

Chapter 1. Organization and Scope of this Dissertation

1.1 CPMV-QD(1.2) Hybrid System as a Bistable Memory Element

In Chapter 2, we develop a substrate based bottom-up approach to assemble two different color emitting quantum dots (CdSe/ZnS core/shell QDs) on the surface of a novel virus mutant, CPMV-T184C. Electrical characteristics of individual hybrids were investigated by conductive atomic force microscopy (CAFM) for potential digital memory applications (i.e. RAM). These individual 40nm CPMV-QD(1,2) hybrids exhibited reversible bi-stable electrical behavior during repeatable writing-reading-erasing processes at the nanoscale.

1.2 CPMV-IO Hybrid as an Scaffold System to Enhanced the Local Magnetic Field Strength of IO Nanoparticles

In Chapter 3, we report the integration of a novel nanoparticle hybrid attained by the covalent attachment of IO (iron oxide, γ-Fe_2O_3) nanoclusters onto the surface of a mutagenized cowpea mosaic virus (CPMV-T184C) nanotemplate.

Combining these two systems (CPMV and IO) was devised as a desirable method to enhance the local magnetic field strength of the IO nanoclusters for their future use in biomedical applications such as magnetic resonance imaging (MRI). Using a stepwise substrate-based integration, monodisperse CPMV-IO hybrids were anchored on a gold substrate. Covalent attachment of the CPMV-IO hybrids was confirmed by FTIR spectroscopy. The physical and magnetic properties of individual CPMV-IO hybrids were qualitatively investigated by atomic/magnetic force microscopy (AFM/MFM). During MFM characterization a ‘boundary-effect’ was observed at the CPMV/IO interface. A strong magnetic field gradient was measured by the magnetic probe and the cantilever experienced a strong attractive force during MFM measurements. This strong interaction at a lift-off distance of 65 nm was indicative of a strong local magnetic field due to a cumulative dipole effect of several IO nanoparticles clustered together.

1.3 $CuInS_2$ Nanowires as a Photosensitive Material

In Chapter 4, we present a novel synthetic route, template assisted sonoelectrochemical deposition to produce crystalline Copper-Indium-Disulfide (CIS) one-dimensional NWs. The effect of the electrolyte’s precursor partial concentrations on the opto-electrical properties of the synthesized NWs is presented here. As-synthesized NWs were characterized spatially by scanning electron microscope; structurally by transmission electron microscope, selected area diffraction and energy dispersive spectroscopy; optically by UV-Vis spectrophotometer and electrically by a semiconductor parameter analyzer and conductive atomic force microscopy.

1.4 Composition Modulated $In_{1-x}Sb_x$ (x~0.5 or 0.7) NWs as Nanowire Field Effect Transistors

In Chapter 5, high quality crystalline $In_{1-x}Sb_x$ NWs are synthesized via a template-based electrochemistry method. Energy dispersive spectroscopy studies show that composition modulated $In_{1-x}Sb_x$ (x~0.5 or 0.7) NWs can be attained by selectively controlling the deposition potential during growth. Single $In_{1-x}Sb_x$ nanowire field effect transistors (NW-FETs) are fabricated to study the electrical properties of as-grown NWs. Using scanning gate microscopy (SGM) as a local gate the I_{ds}-V_{ds} characteristics of the fabricated devices are modulated as a function of the applied gate voltage. Electrical transport measurements show *n*-type semiconducting behavior for the $In_{0.5}Sb_{0.5}$ NW-FET, while a *p*-type behavior is observed for the $In_{0.3}Sb_{0.7}$ NW-FET device. The ability to grow composition modulated $In_{1-x}Sb_x$ NWs can provide new opportunities for utilizing InSb NWs as building blocks for low-power and high speed nanoscale electronics.

Chapter 2. Memory Characterization of CPMV-QD(1,2) Hybrid System by Conductive Atomic Force Microscopy

2.1 Introduction

Viruses and inorganic nanocrystals are ideal nanoparticles that can be modified to exhibit surface properties amenable to nanoassembly for the development of nanoelectronics. Icosahedral viruses, such as CPMV[1,2], are packaged as a highly dense repeat of protein coat subunits within a convenient spherical nanoscale building block. CPMV is also compatible with some organic solvents (e.g. Dimethylformamide), pH and thermally stable[1], and easily extracted and purified[2], serving as a flexible constituent for hybrid nanoassembly. With its known crystal structure[3], hybrid assemblies with CPMV have included conjugation with gold nanoparticles[4,5], gold-coated substrates[6], oligonucleotides[7], and polymer systems[8].

Towards the nanoelectronics end, advanced organic electronic devices based on self-assembled redox molecules[9,10] or nanoparticle incorporated polymers[11,12] have been demonstrated with repeatable conductance switching for memory applications. Previous QD patterning with engineered bacteriophage[13], characterization of CPMV with Au[14], and Tobacco Mosaic Virus for memory[15] show promise for bio-assisted patterning in nanoelectronics. Combining the novel multifunctional capability of viruses and optoelectronic QDs, we show CPMV-QD(1,2) as an exciting material system for electronic memory.

CPMV has a large number of aromatic residues (840 tryptophans per capsid[16]), and the insulating QD capping layer may provide a beneficial barrier for charge transfer. For example, stable electrical bistability with hysteresis was observed in spin coated polyfluorene polymer with an Ag layer[17] and was suggested to be caused by charge transfer between polymer and an intermediate metal layer. Furthermore, nanogold particles with conjugated polyaniline fibers were proposed for memory by an electric field induced charge transfer effect, producing bistable switching as well[18]. Blum et al[19] also showed an increase in conductivity of gold nanoparticle-derivatized CPMV particles after conjugation with conductive molecules. By using a semiconductor instead of a metal, we chose to electrically characterize our CPMV-QD(1,2) hybrid system. Since current hybrid approaches in conjugated organic polymers have reported enhanced charge transfer by the addition of gold nanoparticles[20], we were intrigued by the possibility of a similar effect between a highly aromatic CPMV system and the QDs.

We previously envisioned that solution derived QD-CPMV[21] could be improved upon via a substrate approach, investigating bio-templated assembly of QDs and their electrical characterization for controlled assembly. Using a well characterized, resilient, and labile CPMV-T184C template for QD addition, we have chosen to covalently couple two different color emitting CdSe/ZnS core/shell QDs (QD_{red} and QD_{green}) on the viral capsid, visualizing particle addition by transmission electron microscopy (TEM)[XX], atomic force microscopy (AFM), and electrical characterization by conductive AFM (CAFM). CPMV-T184C mutant provides a uniform distribution of 60 surface cysteines and 300 lysines for multi-site conjugation.

2.2 Materials and Methods

2.2.1 CPMV-QD(1,2) Hybrid System

Using a substrate to initially anchor CPMV-T184C via a SAM crosslinker on Au, followed by a stepwise approach to QD functionalization, aggregation issues are avoided, enabling multifunctional integration of our hybrid system. Initially, SAM on Au deposition was performed using a 1:10 mixture of maleimide disulfide (MED) and hydroxyl-capped disulfide (EG3-EG3) in ethanol. The maleimide functional linker can attach to any protein containing a free cysteine with selective and efficient reactivity at pH ranges of 6.5-7.5[22]. Sulfhydryl ligands form metal complexes to gold with high binding affinity[23]. CPMV-T184C containing 60 cysteines per virion was then introduced to the SAM in the presence of 2 mM tris(carboxyethyl)phosphine (TCEP) reducing agent to produce a viral monolayer. Organic soluble red and green emitting ZnS capped CdSe QDs were hydrophilized by carboxylation and amination to facilitate aqueous based conjugation to the CPMV-T184C surface[21,24]. Green emitting carboxylated QDs (QD_{green}-MAA) were covalently linked to the CPMV-T184C coat protein by activation with EDC (1-Ethyl-3-(3-Dimethylaminopropyl)carbodiimide Hydrochloride) and subsequent attachment to lysine residues.[24,25] Amine functionalized red emitting QDs (QD_{red}-NH_3) were addressed with maleimide groups by reaction with the hetero-bi-functional crosslinker SMCC (Succinimidyl 4-[*N*-maleimidomethyl]cyclohexane-1-

carboxylate)[22,24], and then exposed to the remaining cysteines of the QD_{green}-modified CPMV-T184C particles.

2.3 Characterization of CPMV-QD(1,2) Hybrid System

2.3.1 Surface Characterization by TEM

TEM was used to characterize the viral surface morphologies and demonstrate QD decoration of monodispersed CPMV-T184C (Figure 2.1). The TEM grid was plasma oxidized (Harrick PDC-326 plasma cleaner) to adsorb hybrid lift off solution before imaging at 100kV (FEI-Philips CM300).

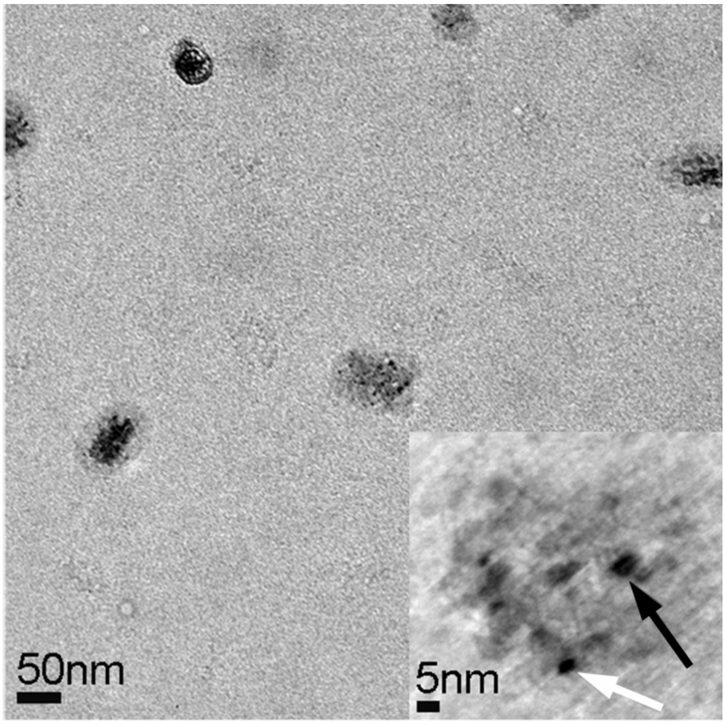

Figure 2.1. TEM of unstained CPMV-QD(1,2) hybrid system thermally lifted off in solution. HRTEM (inset) shows presence of measured ~3.3nm (white arrow) and ~6.1nm (black arrow) QDs in back on a single 30nm CPMV-T184C virus.

Monodispersed CPMV-QD(1,2) hybrids were removed from the Au surface by incubation in water at 50°C for 30 minutes, which is enough to disrupt the Au-S interactions without decomposing the virus particles[1]. Some particles appear less spherical due to possible denatured capsid or flattened viruses on the substrate, and hybrids appear larger than CPMV-T184C due to increased dimension by QD attachment.

The resulting solution was shown by absorbance spectrophotometry at 260nm to contain 38μg/mL of lifted off hetero-bi-functional CPMV-QD(1,2) particles, approximately 80% of total expected yield from the Au substrate (1cm^2 Au area, 100nm $<d>_{CPMV-CPMV}$ spacing, 5.6x10^{6}g/mol).

2.3.2. Composition Characterization by EDX

To spectroscopically verify that the dark regions on each virion shown from the TEM characterization were QDs, EDX spectra was used to identify Cd, Se, Zn, S, elemental peaks consistent with ZnS capped CdSe cored QDs (Figure 2.2). The sharp Cu peak is due to the Cu support of the TEM grid used for analysis. Strong Si peak comes from the Si wafer released from the hybrid lift off procedure.

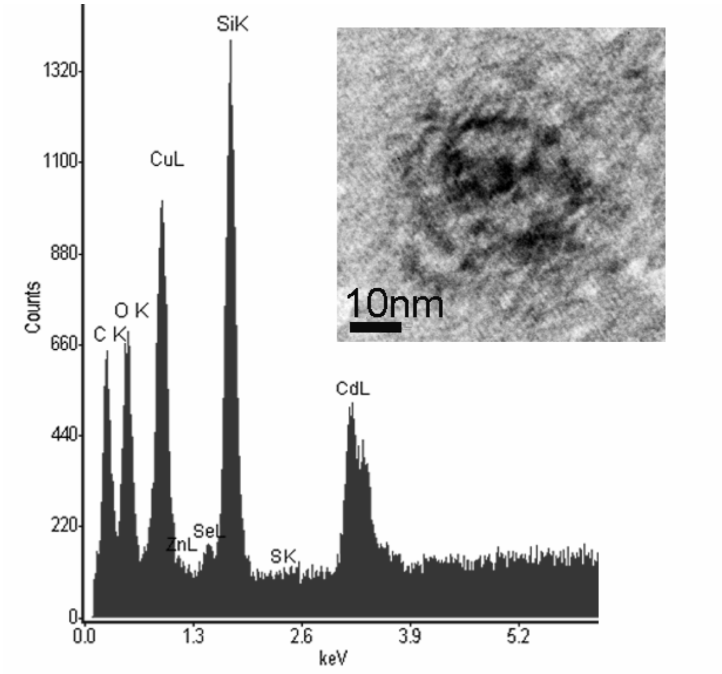

Figure 2.2. Spectroscopy of representative CPMV-QD(1,2) hybrid by Enhanced dispersive X-ray (EDAX) confirming local composition of QD by presence of Cd, Se, Zn, and S elements in the core and capping layer.

2.3.3 Surface Characterization by AFM

Atomic force microscopy in tapping mode was used to characterized the morphology of a monolayer of assembled CPMV-QD(1,2) hybrids on a gold coated silicon (Au/Si) substrate (Figure 2.3). Textured regions throughout the monolayer indicate the location of individual QDs on top of single virions. Inset in Figure 2.3 shows in greater detail the morphology of a single CPMV-QD(1,2) hybrid with dimensions of 40 nm in width and ~10 nm in height. Two different size QDs (QD_{red} and QD_{green}) can also be observed to be attached to its surface, and a cross section on the QD_{red}, shows its dimensions to be ~ 7 nm (width) and 1 nm (height).

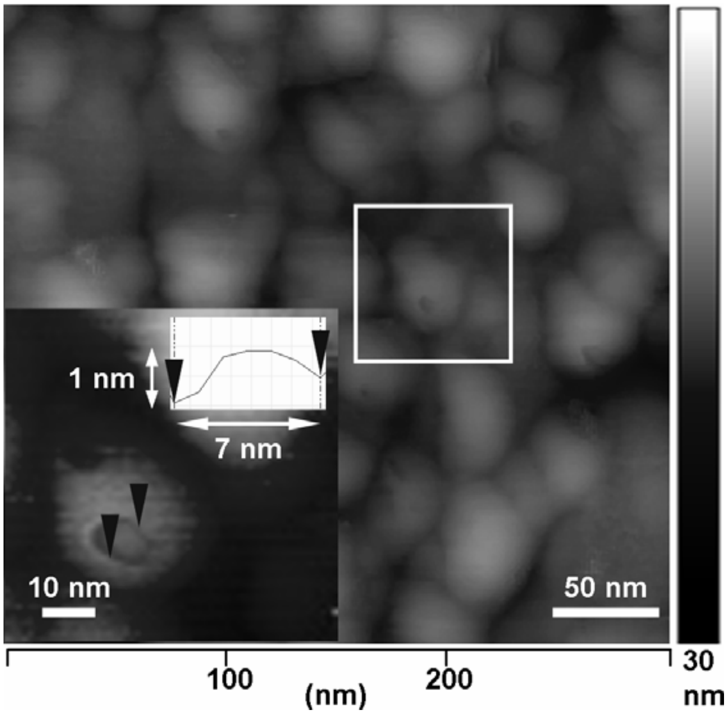

Figure 2.3. Morphology AFM image in tapping mode of monolayer assembled nanoparticle hybrids. Inset shows in greater detail the morphology of a single CPMV-QD(1,2) hybrid and the cross section of a single QD_{red}.

Because a novel nanoparticle hybrid assembly involving the integration of two different size QDs on a single CPMV-T184C virus was developed, it was important to further analyze its morphology to clearly show the different nanomaterials integrating a single hybrid. Figure 2.4 depicts the AFM image in phase mode of the hybrid shown in Figure 2.3 inset. As observed, the QDs can be clearly differentiated from the virion, due to the difference in the tip/sample interaction between the organic (virion) and inorganic (QDs) phase of the hybrid. The sizes of QDs (red and green) are in agreement with those obtained by TEM (7 and 4 nm respectively).

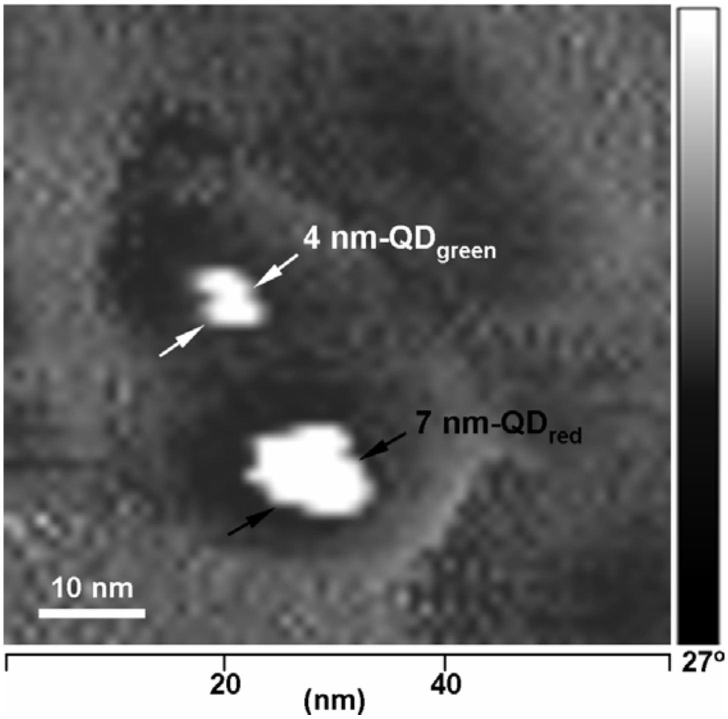

Figure 2.4. Phase AFM image of single CPMV-QD(1,2) hybrid clearly showing two different size QDs (QD$_{red}$ and QD$_{green}$) attached to an individual virion.

2.3.4. Memory Characterization by Conductive Atomic Force Microscopy

All the electrical measurements on single hybrids were performed by Conductive AFM in contact mode under an open air environment and ambient conditions. In a typical electrical characterization experiment, a 'point and shoot' method was used to directly fix a conductive AFM tip (Pt/Ir coated Si tip with a radius of curvature < 20 nm) on a single CPMV-QD(1,2) hybrid. All measurements were carried out by first taking a morphology scan of a monolayer of assembled CPMV-QD(1,2) hybrids and then driving the AFM tip to the top of a single hybrid where a measurement was directly taken across the CPMV-QD(1,2).

For the purpose of the electrical characterization at the nanoscale, the Au/Si substrate was used as the bottom electrode while the stylus of the conductive tip was used as the top electrode with a single CPMV-QD(1,2) hybrid sandwiched in between both contacts as shown in Figure 2.5.

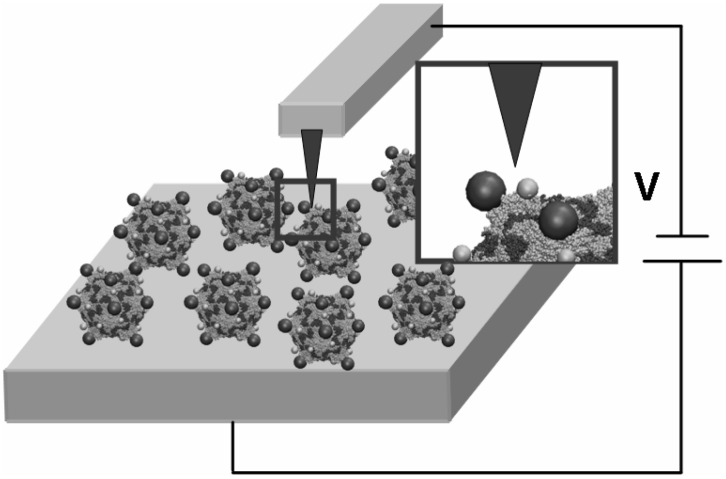

Figure 2.5. Schematic of the setup used for the electrical characterization and implementation of a write-read-erase voltage cycle.

2.4 Results

A total of 100 devices where tested, of which 81 showed bistability behavior. In order to demonstrate that the observed electrical bistability of the CPMV-QD(1,2) hybrid is due to the conjugation of a CPMV-T184C virion and QDs (red and green) rather than an electronic phenomenon caused by either one of the two nanomaterials composing the hybrid, we conducted electrical studies on CPMV-T184C and carboxylated QD_{green} as controls. Figure 2.6 shows that conductance switching is absent in both control samples, supporting the conclusion that the conjugation between both nanomaterials (semiconducting QDs and insulating CPMV-T184C) is important for the observed memory effect.

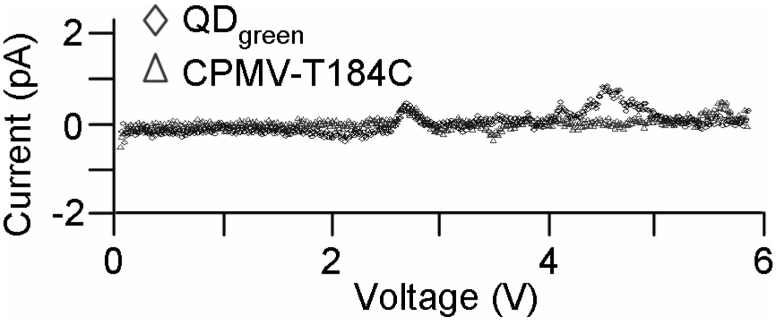

Figure 2.6. I-V curves for CPMV-T184C-only and QD_{green} only configurations showing no switching behavior.

Figure 2.7 shows the I-V characteristics of a typical single CPMV-QD(1,2) hybrid. A memory effect can be observed when a trace and retrace linear voltage scans are applied (-0.5 to 3.0 V and 3.0 to -0.5 V respectively). As observed, the single hybrid is initially in a low conductivity state (defined as OFF state) until it reaches about 2.5 V where a sharp increase in conductivity occurs (defined as ON state), indicating the transition of the device from an initial OFF state to an ON state, equivalent to the 'writing' process in a digital memory element. The hybrid remains at this high conductivity state as the voltage is continuously increased beyond 2.5V.

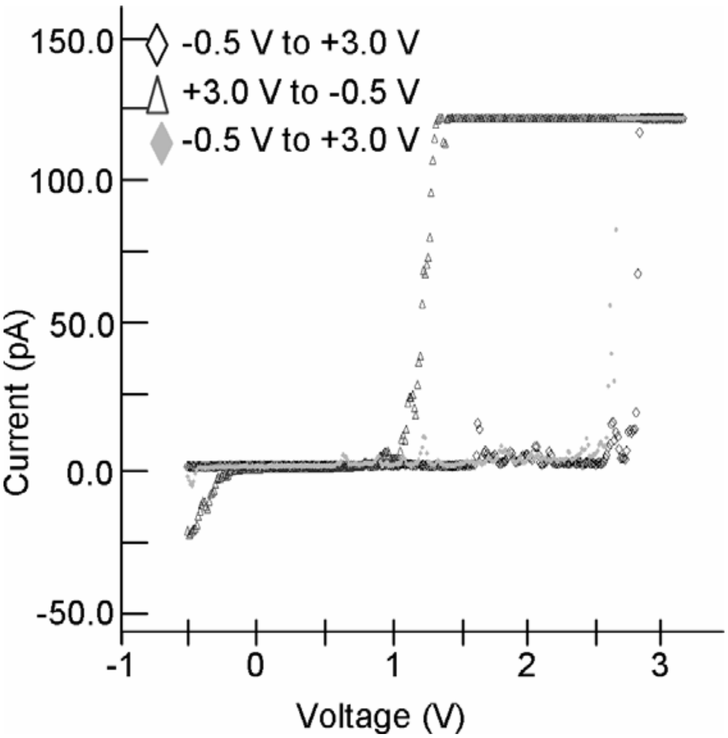

Figure 2.7. I-V characteristics of the CPMV-QD(1,2) hybrid demonstrating its electrical bistability behavior. When a voltage scan from -0.5 to 3.0 V is applied, conductance switching is observed on the CPMV-QD(1,2) hybrid.

Out of 81 devices showing hysteresis, it was observed that seven devices retained a small current value at 0V. The I-V characteristics also show that the single hybrid can return to the initial OFF state by simply applying a reverse voltage bias—equivalent to the 'erasing' process in a digital memory element. A third voltage scan from -0.5 to 3.0 V shows the hybrid’s behavior to be nearly identical to the first voltage scan. This important feature could allow the application of CPMV-QD(1,2) hybrids to be used in a rewritable memory devices. Furthermore, Figure 2.7 is a representative I-V of 33 of the total 81 devices that showed a nanoscale memory effect during CAFM characterization. For these 33 devices, a turn-on voltage of 2.5 ± 0.5V was measured.

Because two different size QDs were used, there are several possible scenarios for the tip/hybrid interaction during CAFM measurements on our CPMV-QD(1,2) hybrids, including (a) tip on red QD only, (b) tip on two interacting QDs (green and/or red), (c) tip on green QD only and (d) tip on virus only without QD at all. The variations in these tip/sample configurations (a-c) affected the turn-on voltage observed in the I-V curves. Using a zero-order approximation, the geometrical details of the interaction of the AFM tip with respect to the hybrid are ignored, and the AFM tip is approximated as a sphere of ~20 nm radius. Figure 2.8 shows superimposed the I-V curves for the three most predominant turn-on voltage regimes, which are believed to be caused by configurations (a-c). For configuration (d) the I-V can be observed in Figure 2.6.

Table 1 associated with Figure 2.8 shows the number of devices (out of 81) that performed under the three main turn-on voltage regimes. Figure 2.9 shows that hysteresis can also be observed under a negative bias.

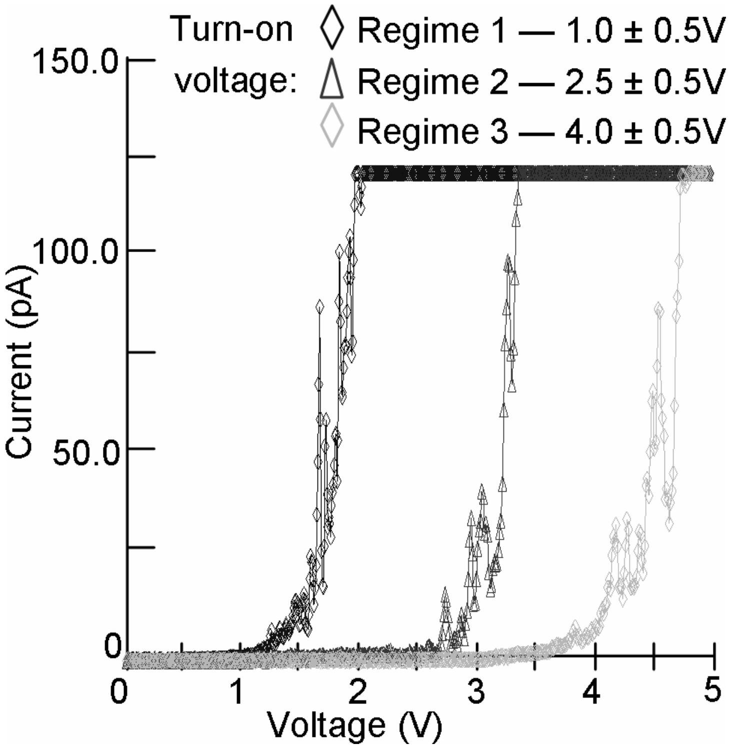

Figure 2.8. I-V curve showing the three most predominant turn-on voltage regimes for the 100 CPMV-QD(1,2) hybrids tested.

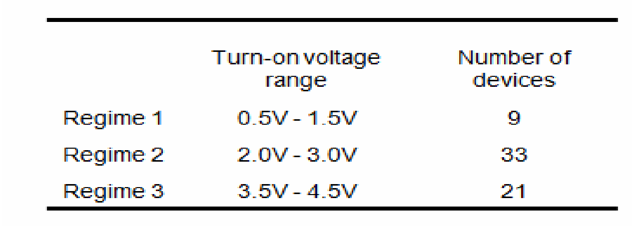

	Turn-on voltage range	Number of devices
Regime 1	0.5V - 1.5V	9
Regime 2	2.0V - 3.0V	33
Regime 3	3.5V - 4.5V	21

Table 1. Turn-on voltage regimes.

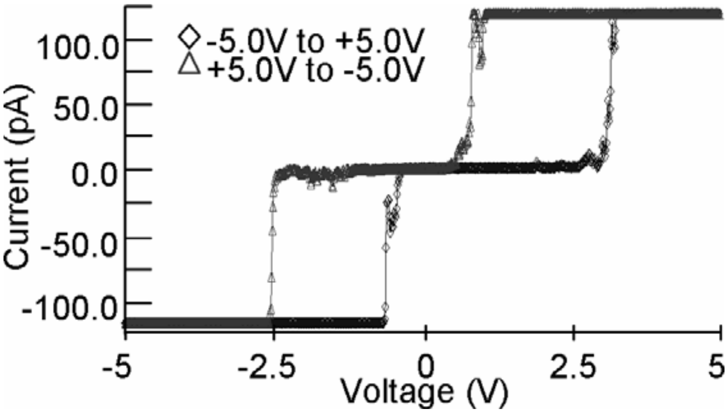

Figure 2.9. I-V curve of a single CPMV-QD(1,2) hybrid under negative and positive bias. I-V shows a comparable electrical bistability under negative bias.

In this hybrid system the QD CdSe core and the CPMV-T184C virus are separated by a high-gap ZnS semiconductor tunneling barrier. Here, the CPMV virus can behave as the charge donor during the conductivity switching allowing charge transfer to the lower-energy core. We suggest in this work, that an E-field induced charge transfer mechanism between the highly aromatic CPMV and the QD core is responsible for the observed electrical bistability of CPMV-QD(1,2) hybrids.

Figures 2.10 and 2.11 show a study on the conduction mechanism in both the ON and OFF states of the CPMV-QD(1,2) hybrid. The plot of log(I) as a function of $V^{1/2}$ (Fig. 2.10) could be fitted to a straight line, and from such linearity it can be observed that the conduction mechanism is probably due to thermionic emission.[26] Therefore, the conduction mechanism in the low conductivity state is dominated by charge injection from the electrode to the CPMV-T184C.

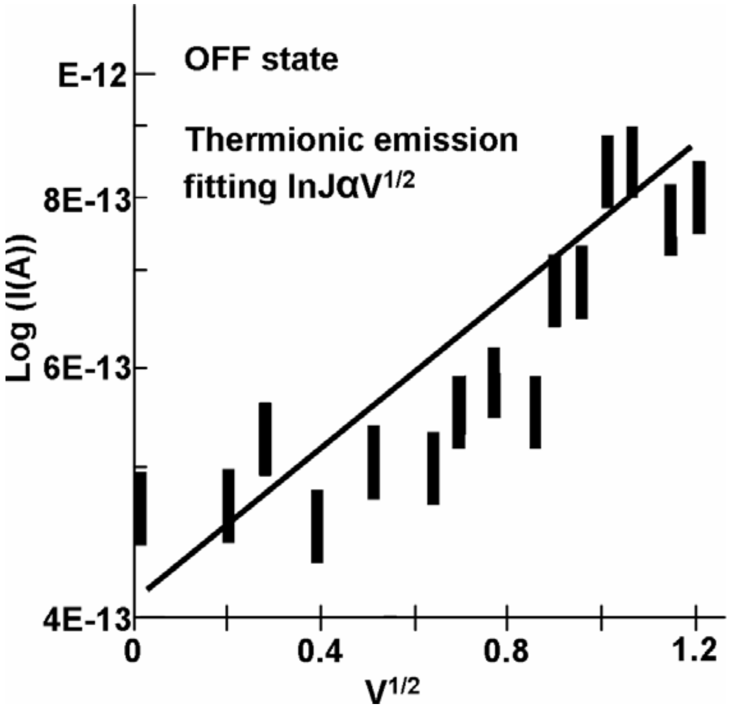

Figure 2.10. Analysis of the I-V characteristics for the CPMV-QD(1,2) hybrid during the low conductivity state.

Furthermore, a linear relation was also observe for the plot of log(*I/V*) as a function of $V^{1/2}$ in the high conductivity state, as shown if Figure 2.11. From this plot it can be observed that a Poole-Frenkel (PF)[27] emission is likely to be the conduction mechanism in the high conductivity state. Increasing to a higher potential helps overcome the high band gap ZnS cap potential barrier by tunneling and injects electrons into the CdSe core. Upon reaching a threshold voltage (i.e. 2.5V), the applied potential enables tunneling into the CdSe core, causing a high conductance switch. Hysteresis was observed in return scanning from high to low bias, suggestive of small charge storage in the QD core.

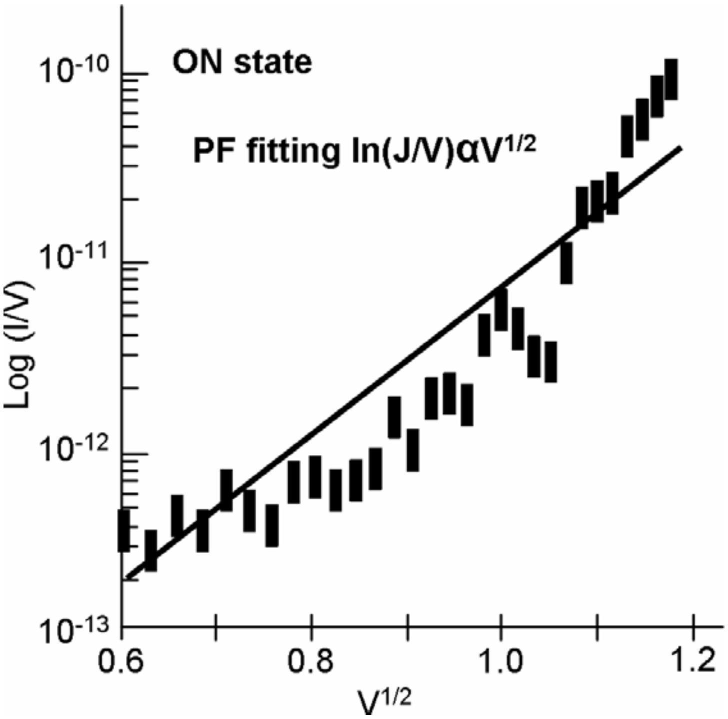

Figure 2.11. Analysis of the I-V characteristics for the CPMV-QD(1,2) hybrid during the high conductivity state.

Furthermore, if the CPMV-QD(1,2) hybrid is to be used in future nanoelectronic devices (i.e. ultra dense memory), it is imperative to demonstrate that a single hybrid can function as an individual single memory element at the nanoscale. Figure 2.12 shows the I-V response of a single hybrid during a typical write-read-erase cycling process that was successfully carried for six complete cycles. During this cycling process, we probed the single hybrid with write, read, and erase voltage pulses of 5.0, 1.5, and -0.5 V, respectively. The corresponding currents to the different voltage pulses were recorded to clearly show the hybrid's switching behavior between two distinct conductance states (ON and OFF).

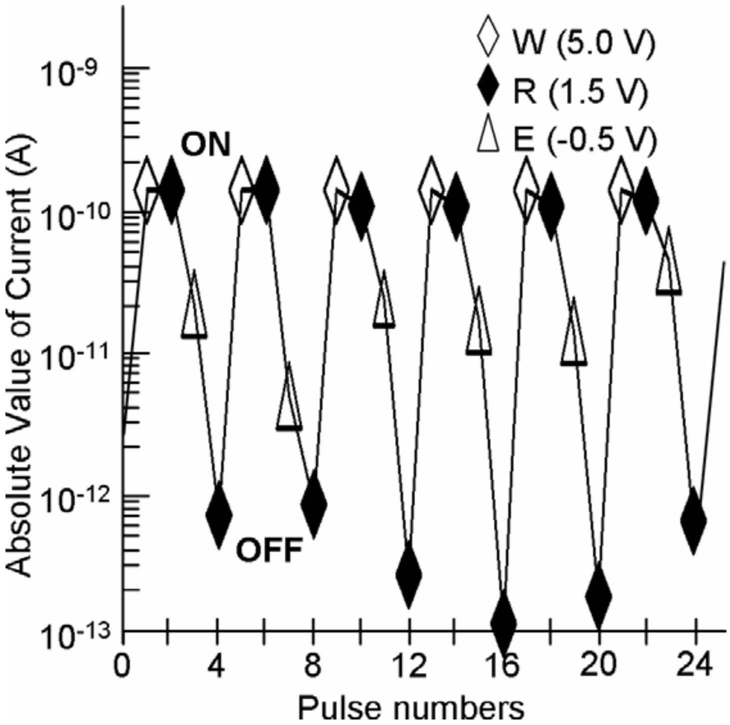

Figure 2.12. I-V response of a single CPMV-QD(1,2) hybrid during write-read-erase voltage cycle (semilog plot).

A characteristic retention time of the ON state was obtained by measuring the conductivity state of the hybrid at one minute intervals (Figure 2.13) after an initial write pulse.

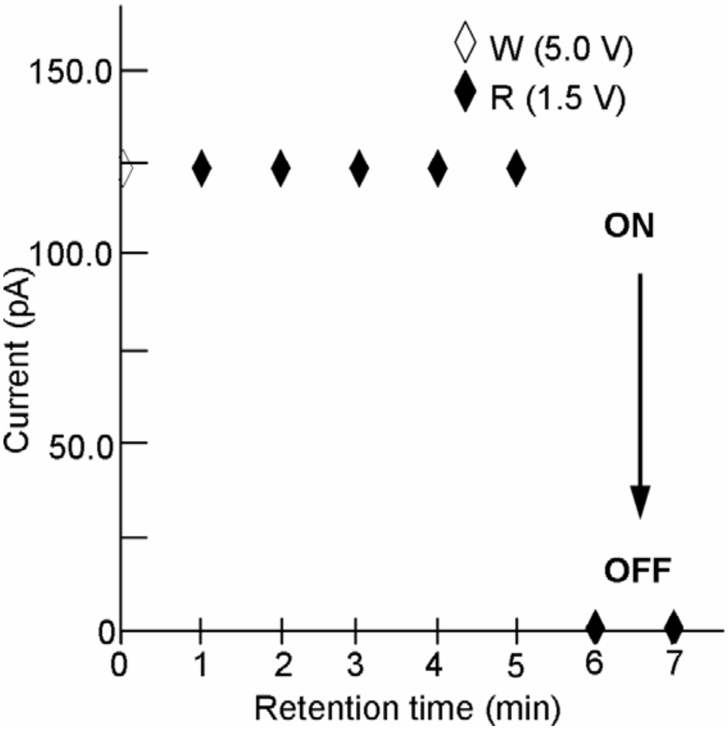

Figure 2.13. Retention time of a single CPMV-QD(1,2) hybrid showing a single initial write and sequential reads at 1 minute intervals.

2.5 Discussion

In the light of these results, we can hypothesize that the current conduction changed from an injection-dominated mechanism in low conductivity state to a charge transport-dominated mechanism in the high conductivity state. In the case of the QD-only control the electric field induced by the applied potential is not enough to allow the charge carriers to tunnel through the QDs. It is therefore, believed that the charge transfer process is the result of the charge donating ability of the CPMV's aromatic residues which enables the observed bistability behavior while it also provides a direct pathway to the charge transfer phenomenon. By analyzing the aromatic residue distribution (Figure 2.14) we can better understand how site attachment is taking place.

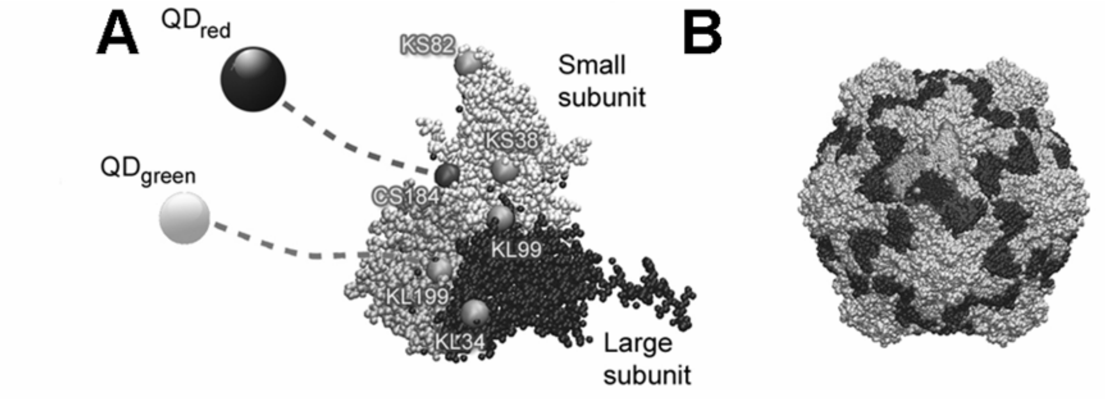

Figure 2.14. Illustration of site selective QD immobilization on the CPMV-T184C virus particle and capsid organization. **(A)** Depiction of site selective QD attachment on CPMV-T184C. **(B)** CPMV capsid is comprised of 60 repeating asymmetric subunits each formed from a large (L) and small (S) coat proteins, arranged in icosahedral symmetry.

At the same time the aromatic distribution, shows a possible source for the charge transfer, where aromatic residues directly overlap with positions of QD attachment (yellow residues in asymmetric subunit), as shown in Figure S2.

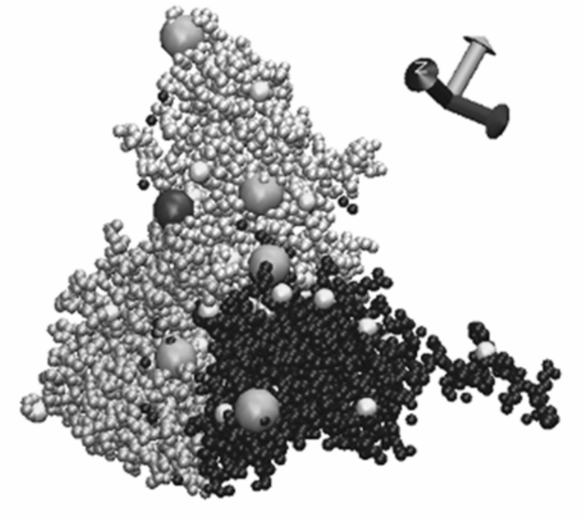

Figure 2.15. Space filling model of asymmetric subunit coat proteins of CPMV-T184C with likely QD binding sites and distribution of solvent exposed aromatic residues in yellow. Aromatic groups overlap with CS184 QD_{red} and KL199 QD_{green}, suggesting a possible source of charge carriers. Three-dimensional axis is located in upper right corner.

Based on the experimental data acquired, a QD size dependence (e.g. bandgap) is observed in the turn-on voltage. Using a first order approximation, these three regimes can be correlated to the number and/or size of the QD(s) across which the current is tunneling through. Therefore, considering that a higher bandgap would require a higher potential to induce tunneling across the CPMV-QD(1,2) hybrid, our results suggest that the three turn-on voltage regimes of 1.0±0.5V, 2.5±0.5V and 4.0±0.5V correspond to the tip/sample configurations (a-c), respectively.

The observed decay of the ON state during the charge retention measurements can be rationalized by two events that take place simultaneously during each measurement. First, because the CPMV-QD hybrid is partially composed of an organic material, the hybrid is inherently susceptible to local Joule heating effects. As such, some degradation of the CPVM-QD interface can be expected to take place each time a high potential is applied to the hybrid. At some point the CPMV-QD interface deteriorates to a point where the device fails to operate. A second plausible explanation deals with a thermionic drifting effect that is experienced by the AFM probe between subsequent electrical measurements. Although for most CAFM based electrical measurements this probe drifting is negligible (<1 nm), in this work the effects can be quite significant due to the nanoscale nature of the measurements and the fact that probing of the CPMV-QD memory behavior is dictated by the interaction between the probe and hybrid.

As shown in Figures 2.7-2.9, 2.12 and 2.13, the high and low conductivity states are repeatable with high accuracy. Furthermore, this ability to write, read and erase the conductivity state of the hybrid accomplishes the functionality of a memory device (i.e RAM) and could expand the applicability of organic-QD hybrids into the realm of memory devices.

2.6 References

1. Virudachalam, R.; Harrington, M.; Markley, J. Thermal Stability of Cowpea Mosaic Virus Components: Differential Scanning Calorimetry Studies. *Virology* **1985**, 146, 138-140.

2. Wang, Q.; Kaltgrad, E.; Lin, T.; Johnson, J. E.; Finn, M. G. Natural Supramolecular Building Blocks: Wild-Type Cowpea Mosaic Virus. *Chemistry & Biology* **2002**, 9, 805-811.

3. Lin T.; Chen, Z.; Usha R.; Stauffacher, C. V.; Dai, J.; Schmidt, T.; Johnson, J. E. The Refined Crystal Structure of Cowpea Mosaic Virus at 2.8 Å Resolution. *Virology* **1999**, 265, 20-34.

4. Wang, Q.; Lin, T.; Johnson, J. E.; Finn, M. G. Natural Supramolecular Building Blocks: Cysteine-Added Mutants of Cowpea Mosaic Virus. *Chemistry & Biology* **2002**, 9, 813-819.

5. Wang, Q.; Lin, T.; Tang, L.; Johnson, J. E.; Finn, M. G. Icosahedral Virus Particles as Addressable Nanoscale Building Blocks. *Angew. Chem. Int. Ed.* **2002**, 41, 459-462.

6. Cheung, C. L.; Camarero, J. A.; Woods, B. W.; Lin, T.; Johnson, J. E.; De Yoreo, J. J. Fabrication of Assembled Virus Nanostructures on Templates of Chemoselective Linkers Formed by Scanning Probe Nanolithography. *J. Am. Chem. Soc.* **2003**, 125, 6848-6849.

7. Strable, E.; Johnson, J. E.; Finn, M. G. Natural Nanochemical Building Blocks: Icosahedral Virus Particles Organized by Attached Oligonucleotides. *Nano Lett.* **2004**, 4, 1385-1389.

8. Raja, K. S.; Wang, Q.; Gonzalez, M. J.; Manchester, M.; Johnson, J. E.; Finn, M. G. Hybrid Virus-Polymer Materials. 1. Synthesis and Properties of PEG-Decorated Cowpea Mosaic Virus. *Biomacromolecules.* **2003**, 4, 472-476.

9. Collier, C. P.; Mattersteig, G.; Wong, E. W.; Luo, Y.; Beverly, K.; Sampaio, J.; Raymo, F. M.; Stoddart, J. F.; Heath, J. R. A [2]Catenane-Based Solid State Electronically Reconfigurable Switch. *Science* **2000**, 289, 1172-1175.

10. Cai, L.; Cabassi, M. A.; Yoon, H.; Cabarcos, O. M.; McGuiness, C. L.; Flatt, A. K.; Allara, D. L.; Tour, J. M.; Mayer, T. S. Reversible Bistable Switching in Nanoscale Thiol-Substituted Oligoaniline Molecular Junctions. *Nano Lett.* **2005**, 5, 2365-2372.

11. Bozano, L. D.; Kean, B. W.; Beinhoff, B.; Carter, K. R.; Rice, P. M.; Scott, J. C. Organic Materials and Thin-Films Structures for Cross-Point Memory Cells Based on Trapping in Metallic Nanoparticles. *Adv. Funct. Mater.* **2005**, 15, 1933-1939.

12. Ouyang, J.; Chu, C. W.; Szmanda, C. R.; Ma, L. P.; Yang, Y. Programmable Polymer Thin Film and Non-Volatile Memory Device. *Nat. Mater.* **2004**, 3, 918-922.

13. Lee, S.-W.; Mao, C.; Flynn, C. E.; Belcher, A. M. Ordering of Quantum Dots Using Genetically Engineered Viruses. *Science* **2002**, 296, 892-895.

14. Blum, A. S.; Soto, C. M.; Wilson, C. D.; Cole, J. D.; Kim, M.; Gnade, B.; Chatterji, A.; Ochoa, W. F.; Lin, T.; Johnson, J. E.; Ratna, B. R. Cowpea Mosaic Virus as a Scaffold for 3-D Patterning of Gold Nanoparticles. *Nano Letters* **2004**, 4, 867-870.

15. Tseng, R. J. ; Tsai, C. ; Ma, L. ; Ouyang, J. ; Ozkan, C. S. ; Yang, Y. Digital Memory Device Based on Tobacco Mosaic Virus Conjugated with Nanoparticles. *Nat. Nanotech.* **2006**, 1, 72-77.

16. Poian, A.; Johnson, J. E.; Silva, J. L. Protein-RNA Interactions and Virus Stability as Probed by the Dynamics of Tryptophan Side Chains. *J. Biol. Chem.* **2002**, 277, 47596-47602.

17. Ouisse, T.; Stephan, O. Electrical Bistability of Polyfluorene Devices. *Organic Electronics* **2004**, 5, 251-256.

18. Tseng, R. J.; Huang, J.; Ouyang, J.; Kaner, R. B.; Yang, Y. Polyaniline Nanofiber/Gold Nanoparticle Nonvolatile Memory. *Nano Letters* **2005**, 5, 1077-1080.

19. Blum, A. S.; Soto, C. M.; Wilson, C. D.; Brower, T. L.; Pollack, S. K.; Schul, T. L.; Chatterji, A.; Lin, T.; Johnson, J. E.; Asminck, C.; Franzon, P.; Shashidhar, R.; Ratna, B. R. An Engineered Virus as a Scaffold for Three-Dimensional Self-Assembly on the Nanoscale. *Small*, **2005**, *1*, 702-706.

20. Ouyang, J.; Chu, C.; Sieves, D.; Yang, Y. Electric-Field-Induced Charge Transfer Between Gold Nanoparticle and Capping 2-Naphthalenethiol and Organic Memory Cells. *Appl. Phys. Lett.* **2005**, 86, 123507-123510.

21. Portney N. G.; Singh, K.; Chaudhary, S.; Destito, G.; Schneemann, A.; Manchester, M.; Ozkan, M. Organic and Inorganic Nanoparticle Hybrids. *Langmuir* **2005**, 21, 2098-2103.

22. Hermanson, G. T. *Bioconjugate Techniques*; Academic Press: San Diego, 1996; pp 148.

23. Bain, C. D.; Troughton, E. B.; Tao, Y.; Evall, J.; Whitesides, G. M.; Nuzzo, R. G. Formation of Monolayer Films by the Spontaneous Assembly of Organic Thiols from Solution onto Gold. *J. Am. Chem. Soc.* **1989**, 111, 321-335.

24. Ravindran, S.; Chaudhary, S.; Colburn, B.; Ozkan, M.; Ozkan, C. S. Covalent Coupling of Quantum Dots to Multiwalled Carbon Nanotubes for Electronic Device Applications. *Nano Letters* **2003**, 3, 447-453.

25. Khorana, H. G. The Chemistry of Carbodiimides. *Chem. Rev.* **1953**, 53, 145-166.

26. Rhoderick, E. H.; Williams, R. H. *Metal-Semiconductor Contacts*, Clarendon, Oxford 1988; pp 80-87.

27. Choudhury, K. R.; Winiarz, J. G.; Samoc, M.; Prasad, P. N. Charge carrier mobility in an organic-inorganic hybrid nanocomposite. *Appl. Phys. Lett.* **2003**, 82, 406-408.

Chapter 3. Local Magnetic Field Strength Characterization of CPMV-IO Hybrid System by Magnetic Force Microscopy

3.1 Introduction

Extensively investigated and mutagenized Cow Pea Mosaic Virus (CPMV) has been demonstrated in a variety of nanoassemblies.[1-3] Iron Oxide (IO) has the potential to surpass limits of detection in bioimaging applications. Particularly γ-Fe2O3 (maghemite) is considered as one of the most desirable materials for technological and biomedical applications due to its inherent biocompatible nature.[4-5] Additionally, maghemite nanoparticles could be directed to an organ, tissue, or tumor using an external magnetic field or heated under an alternating magnetic field.[6-7] Based on the unique magnetic properties of IO nanoparticles they have been extensively used in biomedical applications, such as magnetic resonance imaging, targeting drug delivery and hyperthermia therapy detoxification and cell separation.[8-12]

Combining the two systems can be devised to enhance the local magnetic field strength, by organizing monodisperse IO clusters on a CPMV-T184C mutant viral template. It is known that contrast enhancement is observed by use of superparamagnetic iron oxide nanoparticles (SPIONs) based MRI, by creating large dipolar magnetic field gradients due to their local field inhomogeneity. However, clustering a greater number of IO nanoparticles can further improve contrast beyond free particle SPIONs enhanced MRI, by creating a cumulative dipole effect.[13]

CPMV-T184C is a useful model that has a well characterized structure amenable to surface functionalization.[14] The smallest repeating structure (asymmetric unit, composed of a “small” (24kD) and “large” (42kD) subunit) displays 5 solvent exposed lysines used for IO linkage.[15] By insertion of a cysteine, at residue 184 of the small subunit, anchorage of CPMV to a self assembled monolayer (SAM) on gold substrate pathway can be employed. A previously reported SAM on Au stepwise assembly was used to integrate monodisperse CPMV-IO hybrids for characterization.[16]

It is also been shown that aggregation of Iron oxide particles can exhibit a greater magnetic dipole, and can be suited for in bio-imaging, provided certain properties are met. Harris et al.,[13] demonstrated protease activated aggregation of pegylated iron oxide nanoparticles with enhanced MRI contrast to be most beneficial in improving detection limits of small tumors. Pegylation of CPMV was previously demonstrated to improve circulation times and reduce immunogenicity.[2] Also, based on enhanced permeability and retention effects (EPR),[17] the longest retention times at tumor sites for nanoparticles occurred for 60-400nm.[18] Above 300 nm, there is vulnerability to macrophage phagocytosis,[19] and below 10 nm, nanoparticles can leave the systemic circulation via the lymph nodes.[20] Therefore, the IONs-CPMV nanoparticle hybrid system synthesized and MFM characterized in this report could be used for contrast enhanced MRI applications.

In this work the local enhancement of field strength is studied and demonstrated by magnetic force microscopy (MFM) characterization of CPMV-IO hybrids bound to a substrate by a stepwise assembly process (Figure 3.1).

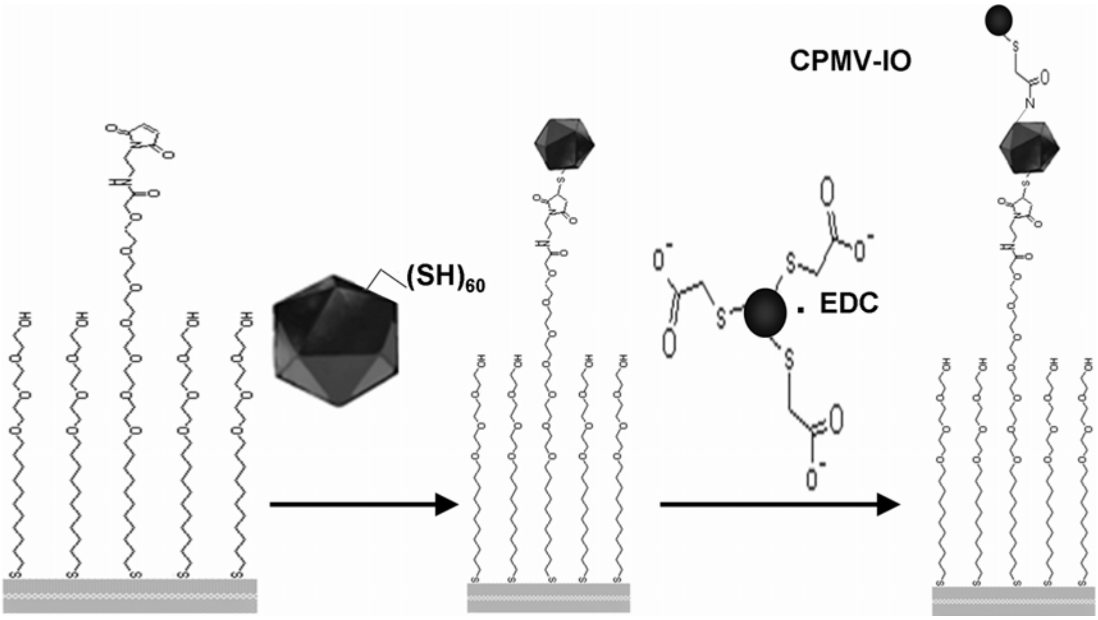

Figure 3.1. Stepwise substrate assembly of CPMV-IO hybrid.

3.2 Materials and Methods

3.2.1 CPMV-IO hybrid system

The synthesis of 11 nm size IO nanoparticles was carried out under nitrogen atmosphere using standard schlenk technique. The biocompatible γ-Fe_2O_3-COOH nanoparticles were synthesized by thermal decomposition of $Fe(CO)_5$ and surface modified as described in detail by Woo et al., [23]. IO nanoparticles protected by oleic acid where synthesized in a 100 mL volume schlenk flask, where oleic acid (1.92 mL, 6.08 μmol) and octyl ether (20 mL) were taken and heated up to 100°C and iron pentacarbonyl (0.40 μmol, 3.04 μmol) was added and continued to reflux for 2 h. The reaction mixture was aerated for 14 h at 80°C and refluxed for another 2 h. In order to obtain the Fe rich surface, nitrogen gas was bubbled into the reaction mixture for 2 h and iron pentacarbonyl (0.04 mL, 0.30 μmol) was added at 100°C and continued to reflux for 1 h. The above reaction mixture was cooled down to ambient temperature. 3-mercaptopropionic acid (0.053 mL, 0.61 μmol) was added to the above mixture and refluxed for 1 h. After cooling down to ambient temperature, excess ethanol was added to isolate IONPs-MPA by magnetic decantation. The mixture of chloroform/methanol/water was added to eliminate the excess surfactant. Pure product of IO nanoparticles tangled with 3-mercaptopropionic acid was isolated using a magnet.

CPMV-T184C was generated by site directed mutagenesis as described by Portney et al., [24]. The chimeric CPMVs were purified from the infected leaves by standard methods described by Dalsgaard et al., with some modifications [25]. Frozen leaves were homogenized in a Waring blender using 0.1 M potassium phosphate pH 7.0, 0.5% ß-mercaptoethanol. After low-speed centrifugation, chloroform-butanol 1:1 was added to the supernatant and stirred for 20 min at 4°C. The aqueous phase was separated by centrifugation and the virus was precipitated using 8% (w/v) polyethylene glycol 8000 and 0.2 M NaCl, stirring for 30 min at 4°C. After centrifugation the virus pellet was resuspended in 0.1 M potassium phosphate pH 7.0 and 0.2 M DTT, and was layered on top of a 30% sucrose solution for ultracentrifugation (42,000 rpm, 3 h at 4°C). The pellet was re-suspended in 3-5 mL of 0.1 M phosphate buffer at pH 7.0 containing 0.1 M DTT. The CPMV particles were further purified on 10-40% sucrose gradients (28,000rpm for 3 h at 4°C). Finally the virus was concentrated and any residual DTT was removed by ultrapelleting the virus through a 30% sucrose cushion (42,000rpm for 3 h at 4°C). CPMV-T184C contains 60 copies each of L and S proteins, with external lysines found at positions 38 and 82 on the small subunit and 34, 99, and 199 on the large subunit, for a total of 300 external lysines per capsid. Cysteines are inserted at position 184 of small subunit, achieving 60 total terminal cysteines per virus.

Deposition of maleimide disulfide/hydroxyl-capped disulfide alkanethiol (MED/EG3-EG3) species was performed by addition of ethanol washed and N_2 gassed Au substrate (Platypus Technologies) into 1 mM MED/EG3-EG3 solution (~2 mL) containing 1.1 mM total disulfide for up to 18 h, followed by another ethanol wash and N_2 drying. MED/EG3-EG3 coated Au substrates were submerged in a CPMV-T184C stock (5 mg mL^{-1}) containing 2 mM tris(carboxy-ethyl)phosphine hydrochloride (TCEP) reducing agent for 1.5 h at RT. Following incubation, removed substrates were successively rinsed in PBS, Tween-20 (1 wt%), and DI water, followed by N_2 gas drying and storage in vacuum. Short reaction times in the presence of TCEP are used to prevent aggregation and saturation of CPMV on substrate, and avoid nonspecific adsorption effects to achieve a homogeneous sample.

Carbodiimide chemistry was used to condense solvent exposed primary amine lysine residues on CPMV-T184C with carboxylated IO [26]. To a solution of IO in PBS buffer (pH=7.5), 50 mM EDC (1-ethyl3-(3-dimethylaminopropyl)carbodiimide hydrochloride) was added to form a highly reactive O-acylisourea intermediate for 15 min, followed by 15 min ester formation with 5 mM sulfo-NHS (N-hydroxysulfosuccinimide) to extend the half life of the carboxylate to hours [27]. Following carboxylate activation, CPMV-T184C coated Au substrate was submersed for 4 h with gentle stirring. Following reaction, substrate was washed with PBS, Tween, and two DI washes before N_2 drying and storage in vacuum.

CPMV-IO nanoparticles hybrids on Au substrate were desorbed by thermal lift off at 50°C for 30 min in 500 uL DI water. Lift off sample (0.044 mg mL^{-1}) was added to plasma oxidized grid using Harrick PDC-326 plasma cleaner.

3.3 Characterization of CPMV-IO Hybrid System

3.3.1 Infrared Spectroscopy Characterization by FTIR

FTIR spectra were obtained by wetting an AgCl window with each sample into instrument (Bruker Equinox 55 FTIR spectrometer). OPUS spectroscopy software was used with 1 cm^{-1} resolution, where a PBS background averaged 20 scans.

Infrared spectroscopy by FTIR supports covalent attachment of CPMV-IO hybrids. Additional amide II bond character due to C-N stretches are dominant in the hybrid (1652 cm^{-1}) and amide I (1648 cm^{-1}) by C=O stretches (Figure 3.2.a).

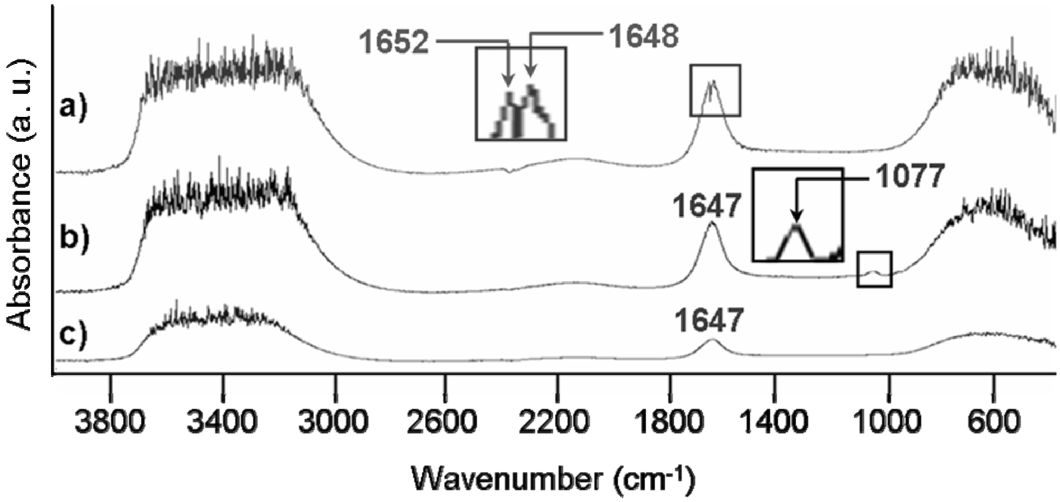

Figure 3.2. FTIR spectroscopy of CPMV-IO hybrids. a) Spectra of CPMV-IO hybrids in PBS solution (pH=7.5). b) Spectra of CPMV-T184C. c) Carboxylated Fe_2O_3 (check) in PBS solution (pH=7.5).

The observed vibrational modes are due to the resonating peptide backbone of the CPMV-T184C capsid,[21] with amide II (C-N) contributed by condensation of carboxylated IO and CPMV-T184C lysines. CPMV-T184C reveals single amide I stretch at 1647 cm^{-1}, a characteristic N-H stretch region (3500-3000 cm^{-1}), and a small RNA peak at 1077 cm^{-1} (Figure 3.2b). Carboxylated IO shows carbonyl C=O stretch at 1647 cm^{-1} (Figure 3.2c). Spectra were obtained using 2 cm^{-1} resolution within blank AgCl windows as the background.

3.3.2 Size Characterization by AFM

AFM imaging was used to characterize structurally the as-synthesized IO nanoparticles on a silicon substrate. A histogram of the size distribution of the IO nanoparticles (Figure 3.3) was determined from 68 individual measurements on single IO nanoparticles exhibited a mean size of ~11 nm. Figure 3.4 shows an AFM image of representative sample used during AFM characterization.

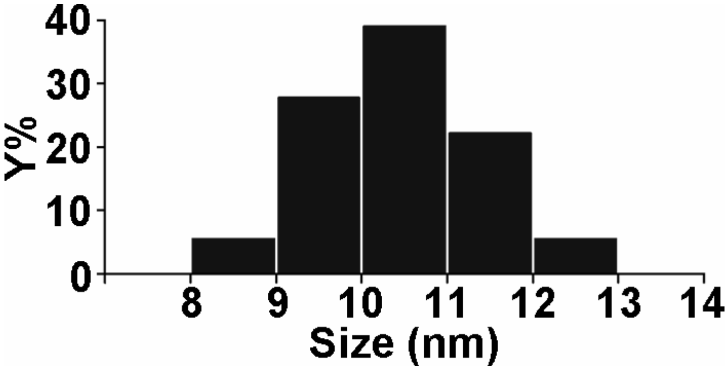

Figure 3.3. Histogram of the measured size distribution for the single IO nanoparticles.

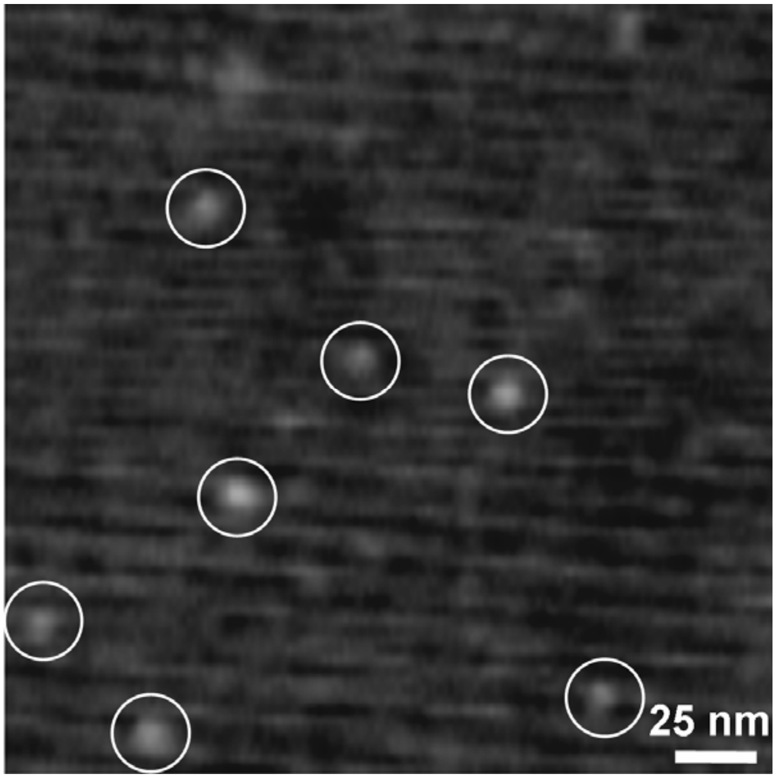

Figure 3.4. AFM topography of as synthesized single IO nanoparticles (white circles).

3.3.3 Size Characterization by TEM

TEM was used to characterize the viral surface morphologies before (inset Figure 3.5) and after (Figure 3.5) integration of IO nanoparticles onto the viral capsid of monodisperse CPMV-T184C mutants. In figure 3.5, the formation of CPMV-IO hybrids can be observed. The structural integrity and spatial organization of IO nanoparticles on the surface of the virions demonstrate the decoration of IO nanoparticles on CPMV-T184C virions. TEM analysis was performed on 400 mesh plain carbon support film on Cu TEM grid (EMS, cat#CF400-Cu) at 100 kV accelerating voltage (FEI-Philips CM300).

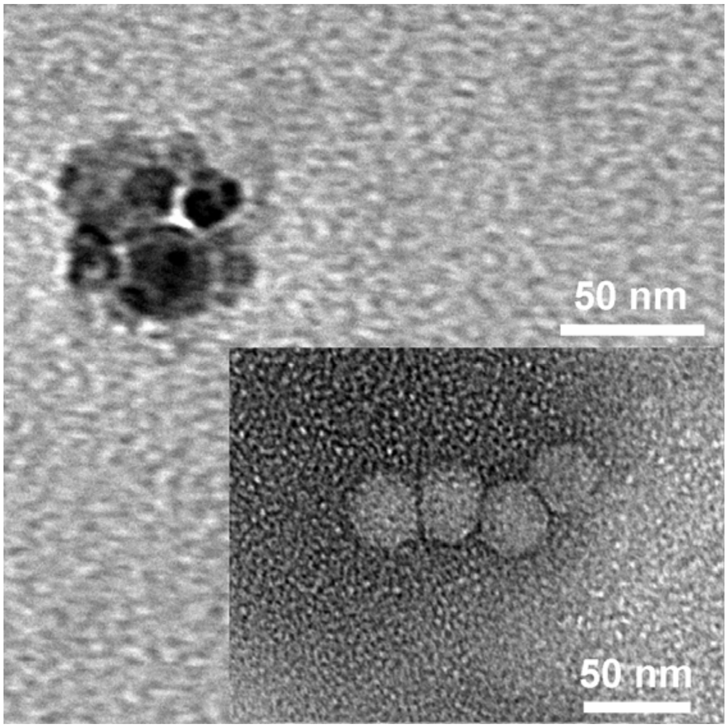

Figure 3.5. TEM of CPMV-IO hybrids recovered after thermal lift-off. Inset shows TEM of individual CPMV-T184C virions**.**

3.3.4 Magnetic Characterization by MFM

MFM experiments were performed with a Multimode V SPM system (Veeco Instruments Inc.). During experimental measurements a magnetic probe (MESP Co/Cr silicon coated tip, ROC ~25 nm) with a resonant frequency 60-100 kHz was used. The nominal spring constant of the cantilever is 2.8 N m^{-1} with coercivity ~400 Oe. MFM measurements were performed in a dynamic lift-mode operation (inset Figure 3.6) at a lift-off distance of 65 nm over the sample, which was optimized in order to reduce the topographical interference and prevent false imaging (i.e. non-magnetic) of the CPMV-

IO hybrids. All measurements were taken under open environment and ambient conditions.

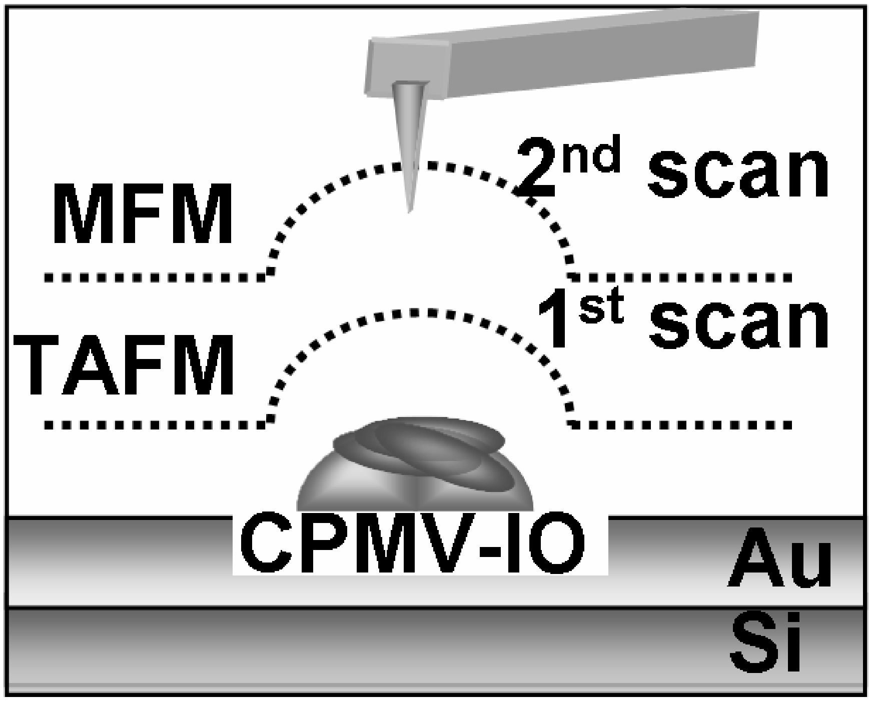

Figure 3.6. AFM/MFM schematic of dynamic lift-mode operation.

3.4 Results

Atomic force microscopy in tapping mode (AFM) and MFM were used to study the topography and magnetic force gradient ($F' = \partial F_z / \partial z$) along the z-axis, respectively. The textured regions observed on each hybrid (Figure 3.7, white selections) are indicative of IO nanoclusters decorating the surface of single virions. Because the two-dimensional array of CPMV-IO hybrids was deposited onto the substrate in a disordered manner, the topography images show very large particles (~200 nm) in the background, consistent with gold grains on the silicon substrate. As discussed above, individual IO nanoparticles were observed and measured to have a nominal size of ~ 11 nm (Figure 2A).

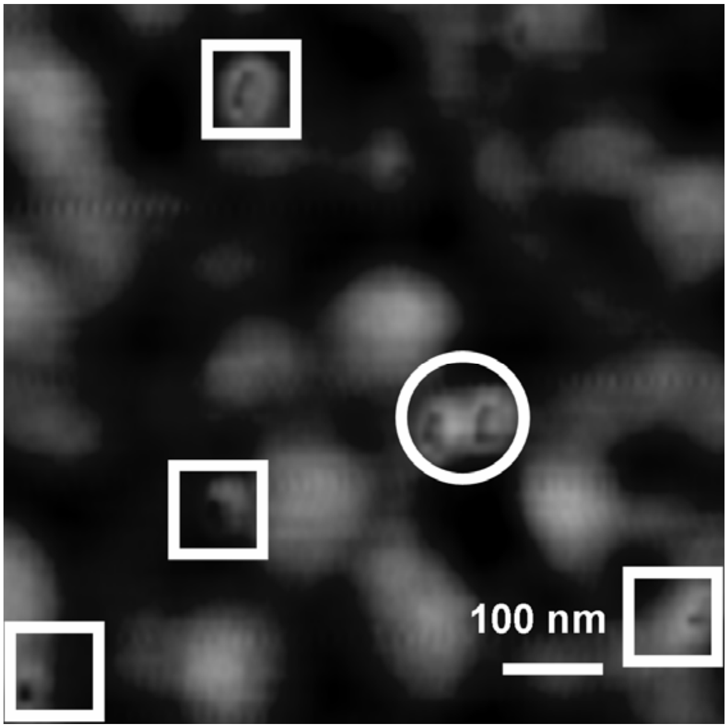

Figure 3.7. AFM topography showing single hybrids (whites squares).

Therefore, in this work it is presumed that each observed IO nanocluster is in fact composed of several single IO nanoparticles. Due to the convolution of the tip with the closely packed individual nanoparticles, these cannot be clearly differentiated from each other but are rather imaged as a nanocluster.

Because in this work the substrate integration of a novel nanoparticle hybrid assembly was developed, it was essential to analyze the morphology to clearly show that two different nanomaterials are integrated in each hybrid. Figure 3.8 provides in greater detail the morphology of a single CPMV-IO hybrid. The cross section (inset Figure 3.8) shows the particle features of CPMV to be ~60 nm, while the IO nanocluster is observed at ~30 nm decorating the surface of the virion.

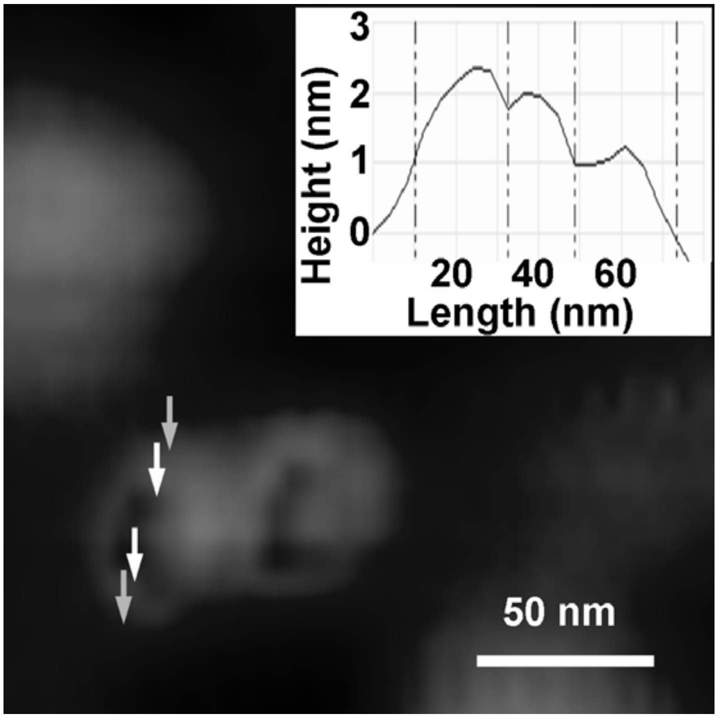

Figure 3.8. AFM topography of two adjacent CPMV-IO hybrids (shown in the white circle of fig. 3.7) and the corresponding cross-section of a single hybrid (inset).

To verify this decoration as a uniquely different nanomaterial system (e.g. IO), phase detection (Figure 3.9) was used. The difference in probe/sample interaction between the organic (CPMV) and inorganic (IO nanocluster) phase of the hybrid revealed that the visco-elastic properties of the IO nanoclusters are essentially different from those of CPMV. The scanning probe experiences a repellent force by the inorganic phase compared to an attractive force by the organic phase (inset Figure 3.9).

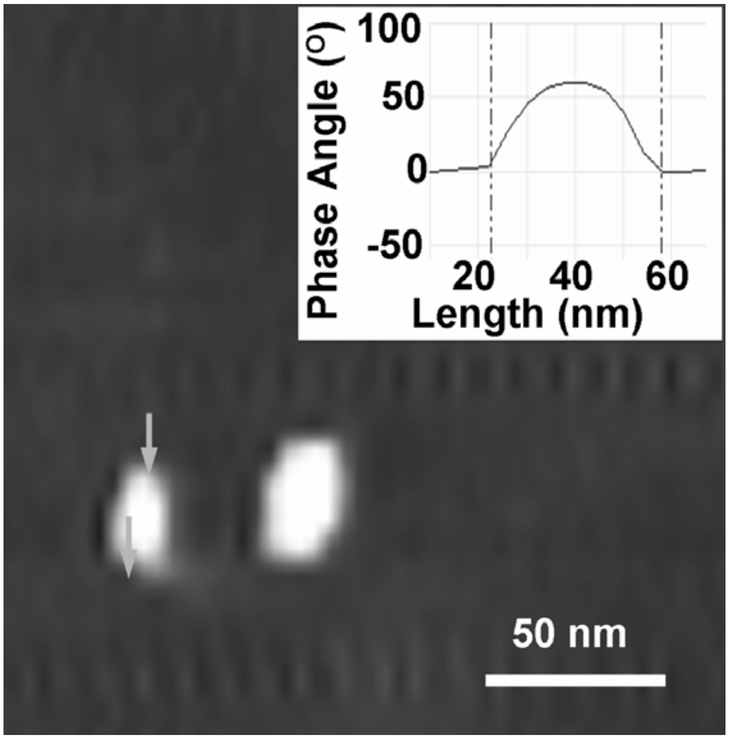

Figure 3.9. AFM phase detection of two adjacent CPMV-IO hybrids (shown in the white circle of fig. 3.7) and the corresponding cross-section of a single hybrid (inset).

AFM phase detection, the magnetic force gradient image (Figure 3.10) shows a very interesting result in which a ‘boundary-effect’ can be observed. MFM measurements show that as the magnetic probe scans the surface of a single hybrid, a repellent force is first exerted on the magnetic probe at the perimeter of the IO cluster.

Although the IO nanocluster is perceived by the probe as a repulsive force in the Then, as the probe moves away from the perimeter and into the inside region of each IO nanocluster a strong magnetic field gradient is measured by the probe and an attractive force is experienced by the cantilever (inset Figure 3.10). A similar "cluster edge effect" was observed by Pedreschi et al.,[22] in the characterization and simulation of colloidal iron nanoparticles. This boundary effect can be hypothesized to be likely due to a symmetry-breaking effect at the perimeter of the IO nanoclusters.

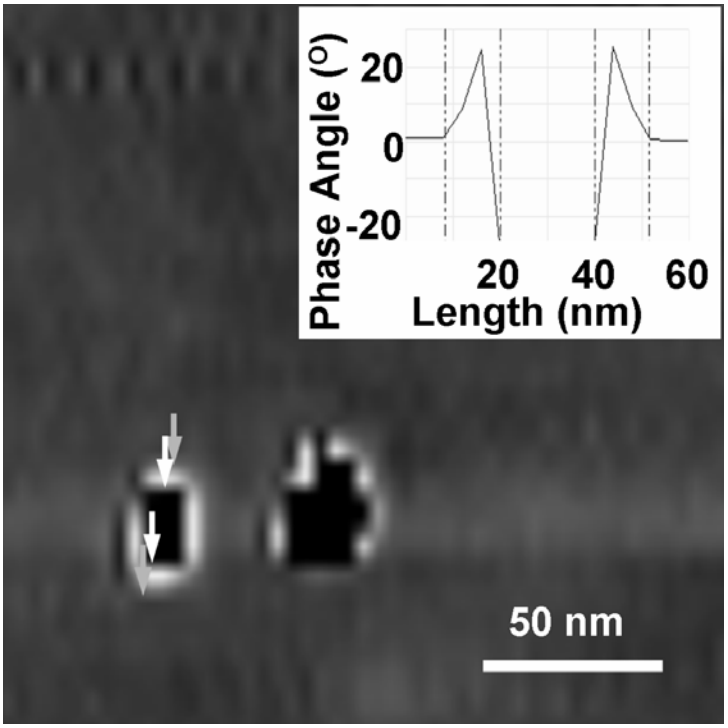

Figure 3.10. MFM phase detection of two adjacent CPMV-IO hybrids (shown in the white circle of fig. 3.7) and the corresponding cross-section of a single hybrid (inset).

Furthermore, when MFM measurements were performed on hybrids with single IO nanoparticles on their surface, the strong magnetic force gradient measured on hybrids containing nanoclusters could not be observed. Figure 3.11 shows a sample area exhibiting both types of hybrids; hybrids with single IO nanoparticles (circles) and hybrids containing IO nanoclusters (squares) on their surface. The cross-section of a hybrid (enclosed by a dark circle in Figures 5.11-5.13) with a single IO nanoparticle shows the size of the nanoparticle to be ~ 12 nm (Inset Figure 3.11).

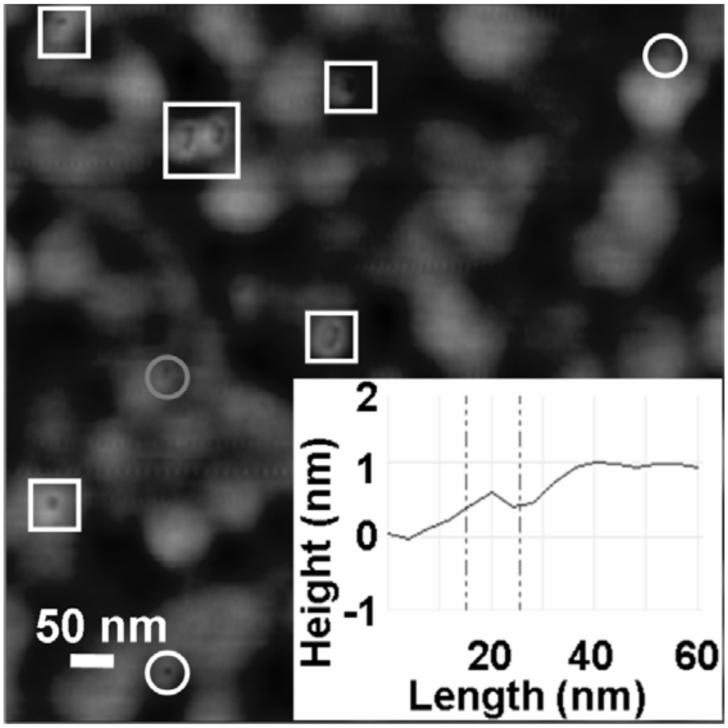

Figure 3.11. AFM topography showing hybrids with single IO nanoparticles (circles) and IO nanoclusters (squares) on their surface. Inset shows the cross-section of single IO nanoparticle on the surface of a single virion (dark circle) as measured by AFM topography.

Meanwhile, no major difference can be observed on the probe interaction with hybrids containing single IO nanoparticles during AFM/MFM phase detection measurements (Figures 3.12 and 3.13, respectively). Cross-sections of a single hybrid during AFM/MFM phase detection measurements (Inset Figures 3.12 and 3.13, respectively) shows that in both cases the probe experiences a slight repulsive force when scanning over the IO nanoparticle. The measured force is comparable in both cases and fundamentally of the same repulsive nature due to the inorganic phase of the hybrid.

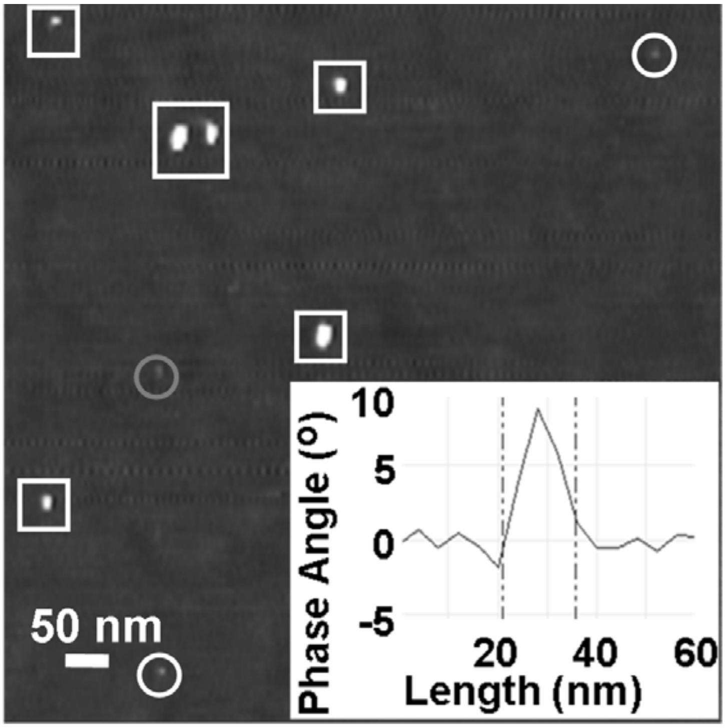

Figure 3.12. AFM phase detection showing hybrids with single IO nanoparticles (circles) and IO nanoclusters (squares) on their surface. Inset shows the cross-section of single IO nanoparticle on the surface of a single virion (dark circle) as measured by AFM phase detection.

In addition, Figure 3.13 shows very clearly that only when the magnetic probe interacts with the hybrids containing IO nanoclusters a strong magnetic field gradient is measured during MFM. This data elucidates the notion that the local magnetic field strength of this hybrid system can be enhanced by covalently attaching (aggregating) IO nanoparticles onto the surface of CPMV-T184C mutants.

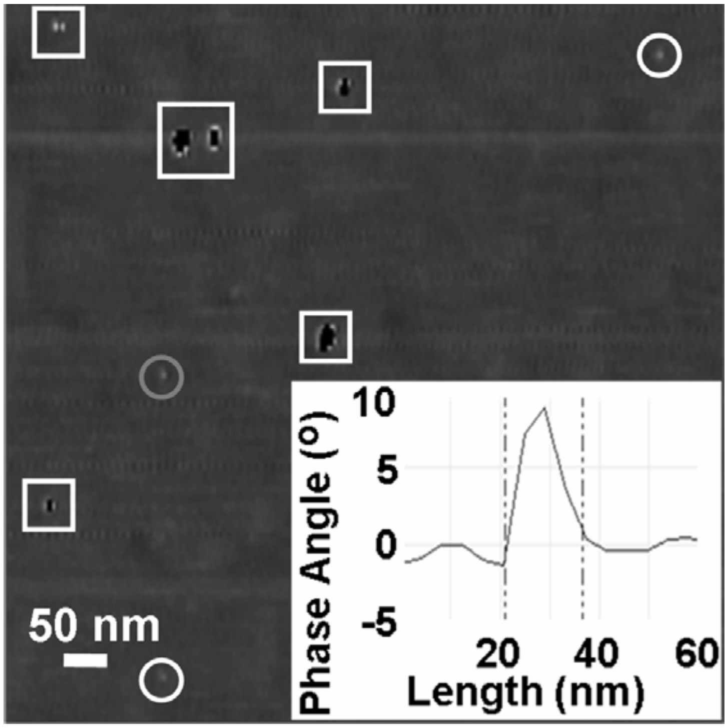

Figure 3.13. MFM phase detection showing hybrids with single IO nanoparticles (circles) and IO nanoclusters (squares) on their surface. Inset shows the cross-section of single IO nanoparticle on the surface of a single virion (dark circle) as measured by MFM phase detection.

During AFM/MFM characterization it was observed that the ratio of hybrids with single IO nanoparticles to hybrids containing IO nanoclusters was 1 to 5. Figures 3.14 and 3.15 show the histograms of the size distribution of IO nanoparticles (Figure 3.14) and IO nanoclusters (Figure 3.15) for both types of hybrids observed in this work.

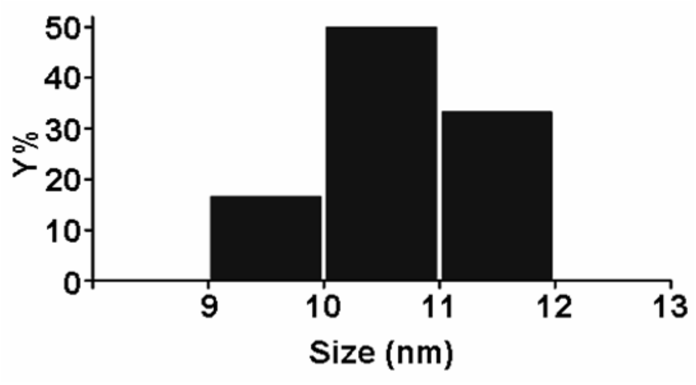

Figure 3.14. Histogram of the measured size distributions of single IO nanoparticles covalently attached to the surface of CPMV-T184C as measured by AFM characterization.

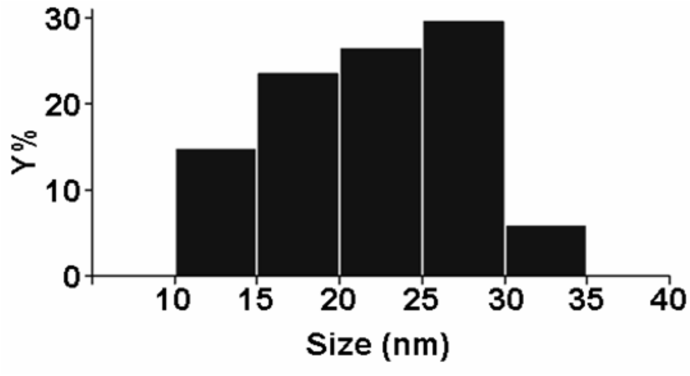

Figure 3.15. Histogram of the measured size distributions of IO nanoclusters covalently attached to the surface of CPMV-T184C as measured by AFM characterization.

The measured size of single IO nanoparticles measured by AFM on the CPMV-IO hybrids is consistent with the size measured of the as synthesized IO nanoparticles before covalent attachment. The results presented here demonstrate the feasibility of covalently attaching IO nanoclusters on an organic scaffold (via substrate based integration) as a mean to enhancing the local magnetic field strength of IO nanoparticles.

3.5 Discussion

To conclude, the enhanced local magnetic field strength was qualitatively analyzed by MFM, demonstrating a characteristic advantage for attaching derivatized magnetic IO nanoparticles in an organic medium. During MFM characterization a ‘boundary-effect’ was observed at the CPMV/IO interface. A strong magnetic field gradient was measured by the probe and the cantilever experienced a strong attractive force during MFM measurements. This strong interaction at a lift-off distance of 65 nm was indicative of a strong local magnetic field most likely due to a cumulative dipole effect of several IO nanoparticles clustered together. Such assembly processes are desirable in tailoring the physical-magnetic properties of a mutant hybrid which could provide multifunctional nanoparticles for enhanced MRI imaging.

3.6 References

1. A. S. Blum, C. M. Soto, C. D. Wilson, J. D. Cole, M. Kim, B. Gnade, A. Chatterji, W. F. Ochoa, T. Lin, J. E. Johnson, B. R. Ratna, *Nano Lett.* **2004**, *4*, 867.

2. K. S. Raja, Q. Wang, M. J. Gonzalez, M. Manchester, J. E. Johnson, M. G. Finn, *Biomacromolecules* **2003**, *4*, 472.

3. Q. Wang, T. Lin, J. E. Johnson, M. G. Finn, *Chemistry & Biology* **2002**, *9*, 813.

4. J. M. Perez, T. O'Loughin, F. J. Simeone, R. Weissleder, L. Josephson, *J. Am. Chem. Soc.* **2002**, *124*, 2856.

5. A. Dyal, K. Loos, M. Noto, S. W. Chang, C. Spagnoli, K. V. P. M. Shafi, A. Ulman, M. Cowman, R. A. Gross, *J. Am. Chem. Soc*. **2003**, *125*, 1684.

6. C. Alexiou, A. Schmidt, R. Klein, P. Hulin, C. Bergemann, W. Arnold, *J. Magn. Magn. Mater*. **2002**, *252*, 363.

7. P. Moroz, H. Pardoe, S. K. Jones, T. G. St Pierre, S. Song, B. N. Gray, *Phys. Med. Biol*. **2002**, *47*, 1591.

8. P. R. Clark, W. Chua-anusorn, T. G. St Pierre, *Magn. Reson. Med*. **2003**, *49*, 572.

9. L. Babes, B. Denizot, G. Tanguy, J. J. Le Jeune, P. Jallet, *J. Colloid Interf. Sci.* **1999**, *212*, 474.

10. R. Hergt, W. Andra, C. G. d'Ambly, I. Hilger, W. A. Kaiser, U. Richter, H.-G. Schmidt, *IEEE T. Mag.* **1998**, *34*, 3745.

11. H. Lee, E. Lee, D. K. Kim, N. K. Jang, Y. Y. Jeong, S. Jon, *J. Am. Chem. Soc*. **2006**, *128*, 7383.

12. A. K. Gupta, S. Wells, *IEEE Trans. Nanobiosci*. **2004**, *3*, 66.

13. T. J. Harris, G. von Maltzahn, A. M. Derfus, E. Ruoslahti, S. N. Bhatia, *Angew Chem. Int. Ed*. **2006**, *45*, 3161.

14. T. Lin, Z. Chen, R. Usha, C. V. Stauffacher, J.-B. Dai, T. Schmidt, J. E. Johnson, *Virology* **1999**, *265*, 20.

15. Q. Wang, E. Kaltgrad, T. Lin, J. E. Johnson, M. G. Finn, *Chemistry & Biology* **2002**, *9*, 805.

16. N. G. Portney, R. J. Tseng, G. Destito, E. Strable, Y. Yang, M. Manchester, M. G. Finn, M. Ozkan, *Appl. Phys. Lett.* **2007**, *90*, 214104.

17. H. Maeda, T. Sawa, T. Konno, *J. Control Release* **2001**, *74*, 47.

18. D. P. O'Neal, L. R. Hirsch, N. J. Halas, J. D. Payne, J. L. West, *Cancer Lett.* **2004**, *209*, 171.

19. T. R. Green, J. Fisher, M. Stone, B. M. Wroblewski, E. Ingham, *Biomaterials* **1998**, *19*, 2297.

20. S. M. Moghimi, A. C. Hunter, J. C. Murray, *Pharmacol. Rev*. **2001**, *53*, 283.

21. H. H. Mantsch, D. Chapman, *Infrared Spectroscopy of Biomolecules*, Wiley-Liss Inc., New York, USA **1996**, p. 239.

22. F. Pedreschi, J. M. Sturm, J. D. O'Mahony, C. F. J. Flipse, *J. Appl. Phys*. **2003**, *94*, 3446.

23. K. Woo, J. Hong, *IEEE Trans. on Magnetics* **2005**, *41*, 4137.

24. N. G. Portney, A. A. Martinez-Morales, M. Ozkan, *ACS Nano* **2008**, *2*, 191.

25. K. Dalsgaard, A. Uttenthal, T. D. Jones, F. Xu, A. Merryweather, W. D. O. Hamilton, J. P. M. Langeveld, R. S. Boshuizen, S. Kamstrup, G. P. Lomonossoff, C. Porta, C. Vela, J. I. Casal, R. H. Meloen & P. B. Rodgers, *Nat. Biotechnol*. **1997**, *15*, 248.

26. H.G. Khorana, *Chem. Rev.* **1953**, *53*, 145.

27. G. T. Hermanson, *Bioconjugate Techniques*, Academic Press, San Diego, USA **1996.**

Chapter 4. Effect of electrolyte concentrations on the opto-electrical properties of sonoelectrochemically deposited Copper-Indium-Disulfide NWs

4.1 Introduction

The ternary compound semiconductor Copper-Indium-Disulfide (CIS) is one of the more promising candidates as an absorber layer for photovoltaic devices due to its low cost and high efficiency.[1-3] Power conversion efficiencies of up to 12% for thin film devices have been achieved.[2] The band gap (Eg = 1.5 eV) is well matched with the solar spectrum and the components are available in abundant quantities.[4] An additional advantage of CIS, over similar materials like CdTe or CdS, is it's low toxic potential.[3] Recently, lot of thrust has been given on the development of solar cells based on one-dimensional (1-D) nanostructures,[5-7] which are more advantageous than the conventional thin film solar cells due to their better charge directionality and larger surface area for production of excitons.[8] Therefore, currently there is an increasing interest in developing CIS NWs, but up to date only solvothermal synthetic methods has been reported in the literature for CIS 1-D nanostructures.[9-13] This process requires high temperatures and time consuming steps. In this work, a simple way of synthesizing crystalline, semiconducting copper-indium-disulfide one-dimensional nanostructures by using ultrasonication during template assisted electrodeposition is reported. We have recently developed this technique and utilized it to successfully synthesize high structural quality copper sulfide nanorods.[14] The major advantages of sonoelectrochemical deposition are low operating temperature, less time consumption, high reproducibility, better shape/size controllability and high structural quality of the product.[14]

It has been reported for thin films that relative concentration of copper (Cu) and indium (In) play an important role in determining their opto-electrical properties but a similar observation has not been made for NWs.[15,16] This is an issue of great importance for the employment of these NWs in future photovoltaic devices. In this work we have observed the effect of electrolyte composition on the properties of electrodeposited CIS NWs

4.2 Materials and Methods

4.2.1 Sonoelectrochemistry deposition of CIS NWs

The synthesis process of template assisted sonoelectrochemical deposition of NWs has been described in details in our previous work.[14] In short, electrolyte with two different precursor compositions was prepared. The copper salt rich solution ($CuSO_4$: 100 mM, In_2S_3: 60 mM) was termed as 'C-rich', while indium salt rich solution ($CuSO_4$: 60 mM, In_2S_3: 100 mM) was termed as 'I-rich'. The concentration of sulphur salt was kept constant in both ($Na_2S_2O_3$: 400 mM) C-rich & I-rich solutions. The sonoelectrodeposition was performed at room temperature and open air environment. Isopore (Millipore) Polycarbonate (PC) template (200 nm pore size) was used as the working electrode in a three electrode electrochemical cell with Ag/AgCl and Pt wire as the reference and counter electrodes, respectively. During the sonoelectrochemical deposition process, a constant -1 V potential was applied between the counter and working electrodes. At the end of the deposition process, the NWs were freed by dissolving the PC template in chloroform. The samples used for optical and electrical characterization were prepared by cleaning the solution by ultracentrifugation.

4.3. Characterization of CIS

The morphology and structure of the as-synthesized NWs were characterized by scanning electron microscopy (SEM, Leo Supra55, E = 15 kV). Selective area electron diffraction (SAED) patterns of the NWs were studied by transmission electron microscopy (TEM, FEI-Philips CM300, E = 300 kV). Energy dispersive x-ray (EDX) analysis was employed to analyze the chemical composition of the as-synthesized nanostuctures. Absorption spectra was measured in the wavelength region λ = 350-1000 nm using a UV-Vis spectrophotometer (Perkin Elmer Lambda 35) at room temperature. Electrical measurements and field effect studies were conducted by a semiconductor parameter analyzer while radial I-V measurements were done by conductive atomic force microscopy (C-AFM, Veeco, MultiMode V Scanning Probe Microscope) under open air and ambient conditions.

One-dimensional CIS nanostructures with good structural uniformity and high aspect ratios were prepared by template assisted sonoelectrochemical deposition. SEM characterization of the as-synthesized C-rich and I-rich samples is shown in figures 4.1 and 4.2 respectively. The SEM images indicate that the as-synthesized products are well defined NWs with diameters of ~200 nm and lengths ranging from 2 to 10 μm. The upper inset in figures 4.1 and 4.2 show in greater detail the surface structure (i.e. roughness) of the as-synthesized NWs and structurally no major structural differences can be observed between the two.

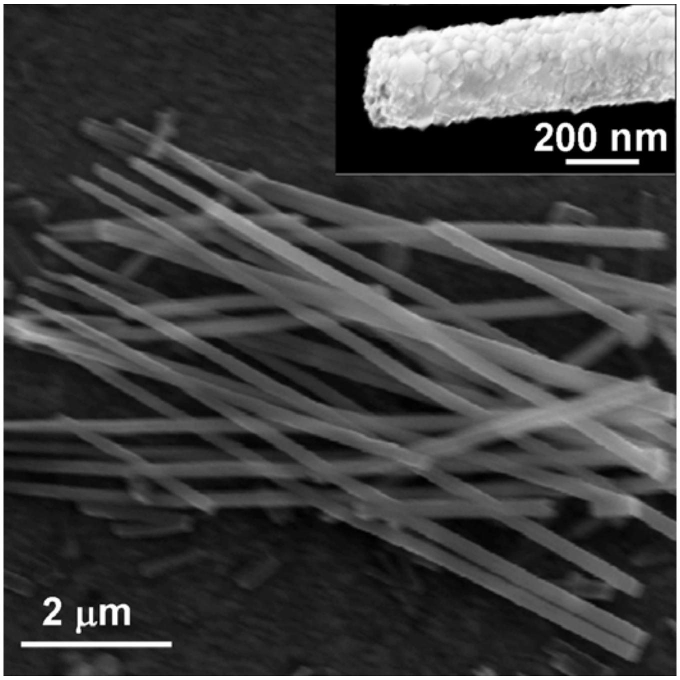

Figure 4.1. Low-magnification SEM of C-rich CIS NWs synthesized by sonoelectrochemistry. Inset shows a high-magnification SEM of a representative single C-rich NW.

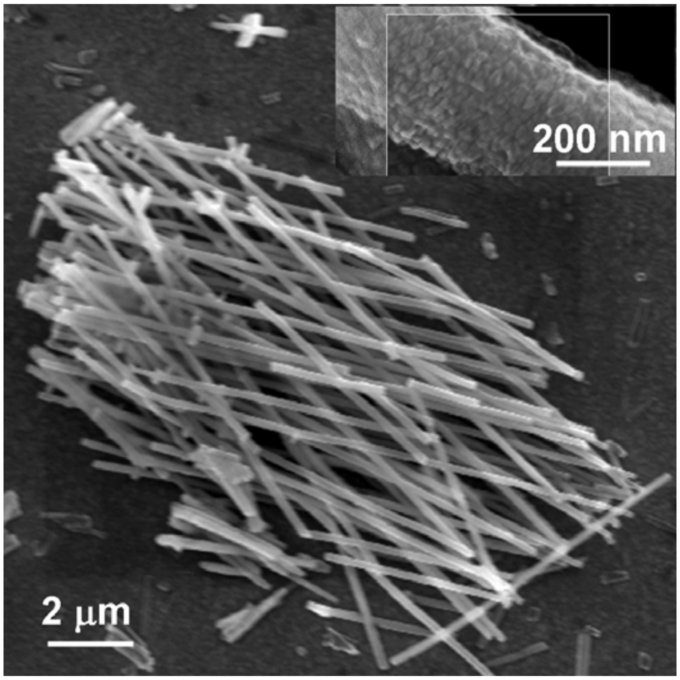

Figure 4.2. Low-magnification SEM of I-rich CIS NWs synthesized by sonoelectrochemistry. Inset shows a high-magnification SEM of a representative single I-rich NW.

The crystal structure of the deposited NWs was examined by TEM and SAED. The inset of figures 4.3 and 4.4 are typical TEM micrograph images of the as-synthesized products. The discrete spots recorded by SAED (Figures 4.3 and 4.4) show the crystalline structure of the NWs along the [-3-21] and [-123] zone axis for the C-rich and I-rich samples, respectively.

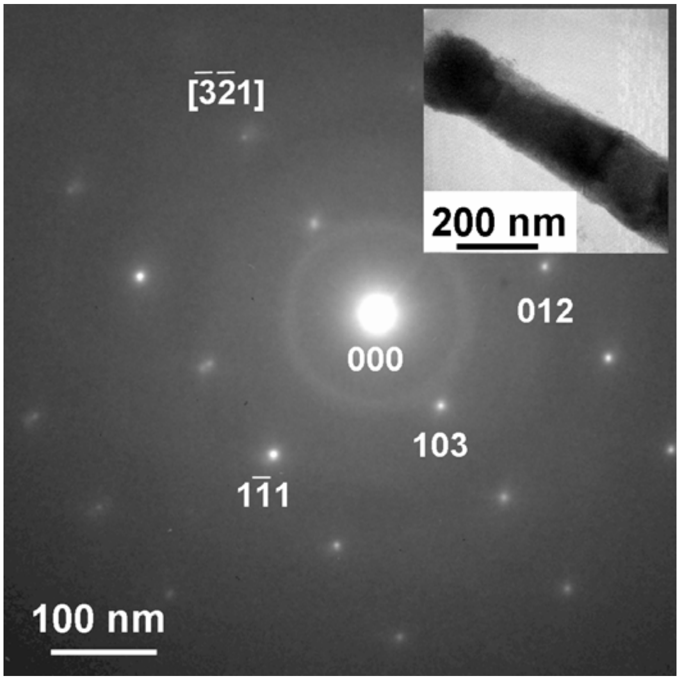

Figure 4.3. SAD pattern of as-synthesized C-rich NW. Discrete spots obtained indicate the crystalline nature of the electrochemically grown NW.

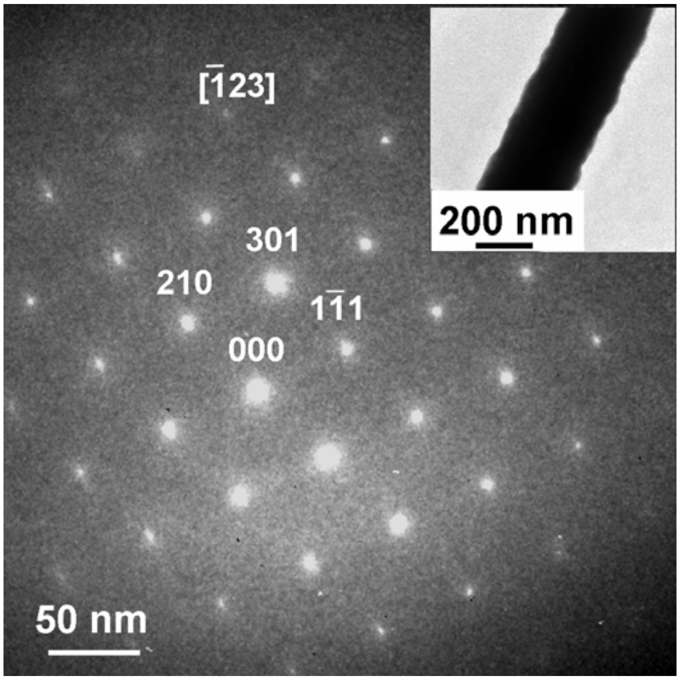

Figure 4.4. SAD pattern of as-synthesized I-rich NW. Discrete spots obtained indicate the crystalline nature of the electrochemically grown NW.

In addition, EDX analysis on single NWs from each sample product, allowed us to confirm that their composition is made up of copper, indium and sulfur as determined by their corresponding emission energy spectrum (Figures 4.5 and 4.6). Although the atomic ratios for each sample (C-rich: Cu/In ~ 3.03, I-rich: In/Cu ~ 3.10) determined by EDX spectra are more qualitative in nature than quantitative, and HRTEM coupled with EDX analysis of a reference sample is required to determine exact composition; they clearly prove that the C-rich sample and the I-rich sample are more abundant in copper and indium respectively.

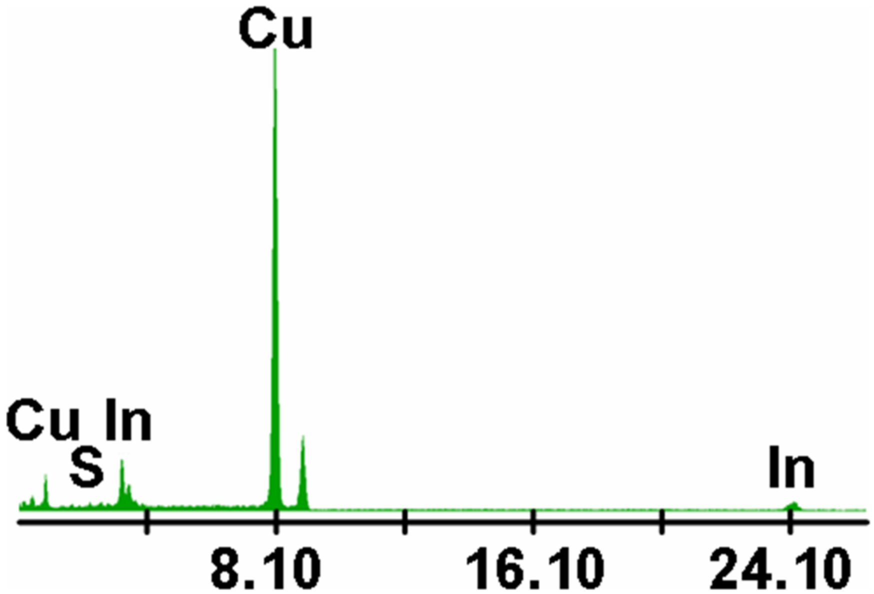

Figure 4.5. EDS spectra corresponding to a C-rich NW.

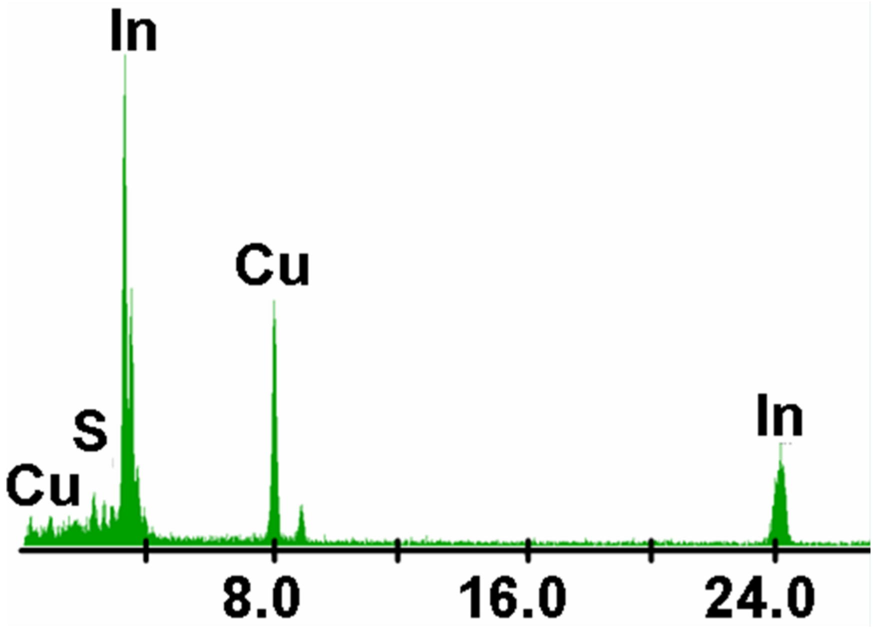

Figure 4.6. EDS spectra corresponding to a I-rich NW.

As discussed in great detail in our previous work,[14] one of the major advantages of combining ultrasonication with electrodeposition is the vast improvement in the structural quality of synthesized NWs. Ultrasonication improves the quality and growth rate of NWs deposited in the template by the process of cavitation, which is the formation, growth and implosive collapse of bubbles inside the liquid.[17,18] The collapse of these bubbles inside the liquid generates intensive shock waves, and the transient high pressure from the shock waves helps to prevent the plugging of the nanopores enhancing mass transfer rate.[17] Additionally, ultrasonic waves generate very high acoustic pressures which produces an acoustic capillary effect (i.e. the rate of liquid streaming is considerably accelerated inside the thin capillaries under the effect of ultrasound).[18] The decrease in overpotential and increase in electrolyte temperature also help in increasing the deposition rate and structural quality.[19] This effect of ultrasonication on deposited NWs was also observed in CIS NWs as well; both types of NWs, C-rich & I-rich, were found to be crystalline in nature. These results also show that sonoelectrochemical deposition is independent of the chemical composition of the system being electrodeposited and could be used in deposition of high quality of NWs of other materials.

4.4 Results

CIS is primarily used for developing solar cells and hence the optical properties of these NWs are of great importance. The obtained spectra (Fig. 3) were similar to those previously reported for CIS nanostructures.[9] A slight difference in the peak position among samples C-rich and I-rich was observed. For the C-rich sample a peak was observed around 377 nm, while for the I-rich sample a peak was observed around 380 nm, indicating that both NWs have a deeper absorbance compared to the bulk material. This observation is very important for the application of these NWs in optical devices utilizing light absorption properties of their components.

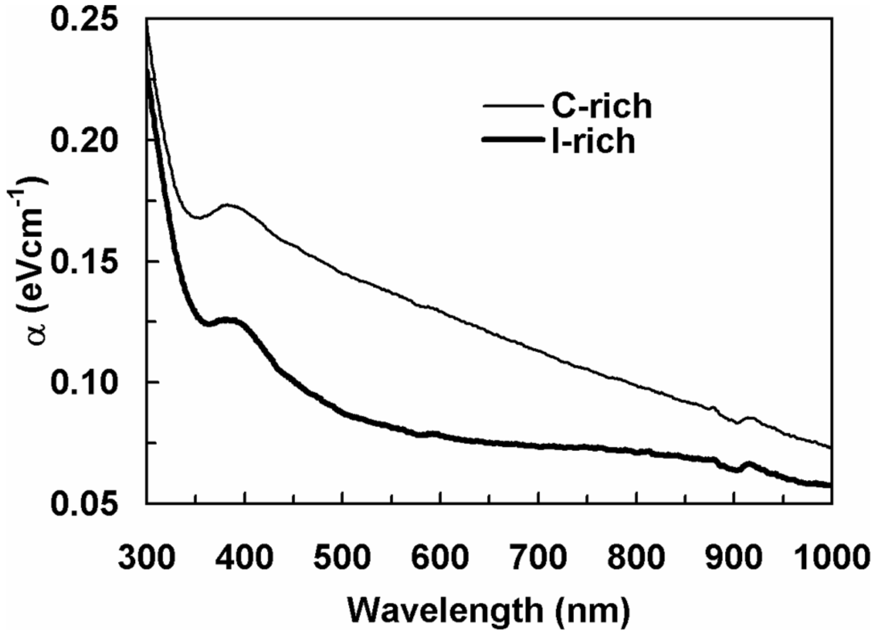

Figure 4.7. Absorption spectra of C-rich and I-rich NWs recorded at room temperature (light and dark curves, respectively). A peak at 377 nm is observed for C-rich, while a peak at 380 is observed for I-rich.

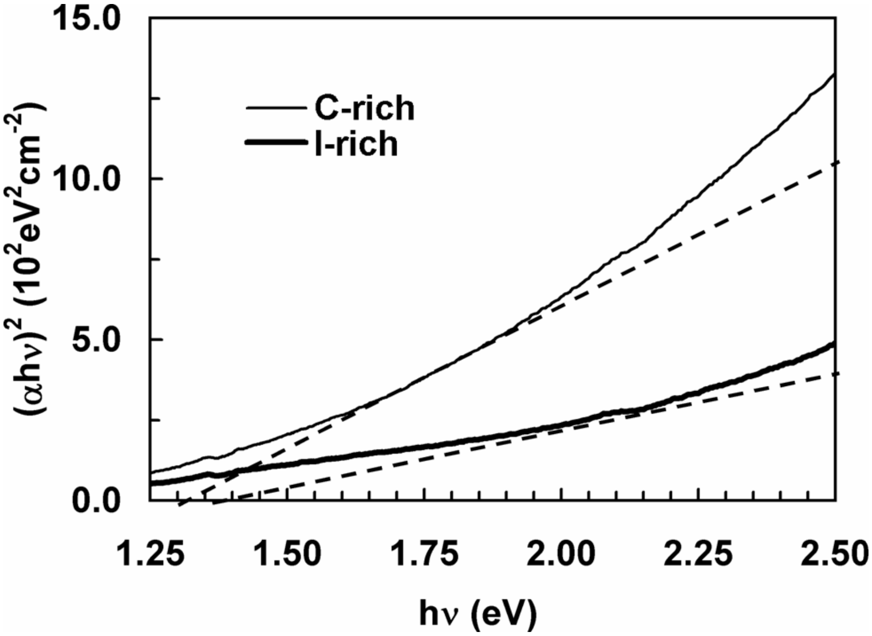

Figure 4.8. Absorption spectra of C-rich and I-rich NWs vs. photon energy.

Due to the great importance of semiconducting NWs in the application of future nanoscale optoelectronic devices,[20,21] it is imperative to characterize the electrical transport properties of as-synthesized CIS NWs for their potential application in nanoelectronics.[22,23] However, to the best of our knowledge, there have been no reports on the opto-electrical characteristics of copper-indium-sulfide NWs. To study the electrical transport properties and ascertain their semiconducting nature, a field effect transistor (FET) device based on an individual CIS NWs (D ~ 200 nm, L ~ 2 μm) was fabricated on an oxidized Si substrate (50 nm SiO_2 layer) by drop casting the NWs on pre-patterned gold electrodes.[14] Ohmic contacts to the source and drain were fabricated by focus ion beam (FIB). The wafer was used as a back gate throughout the FET measurements (Figure 4.9).

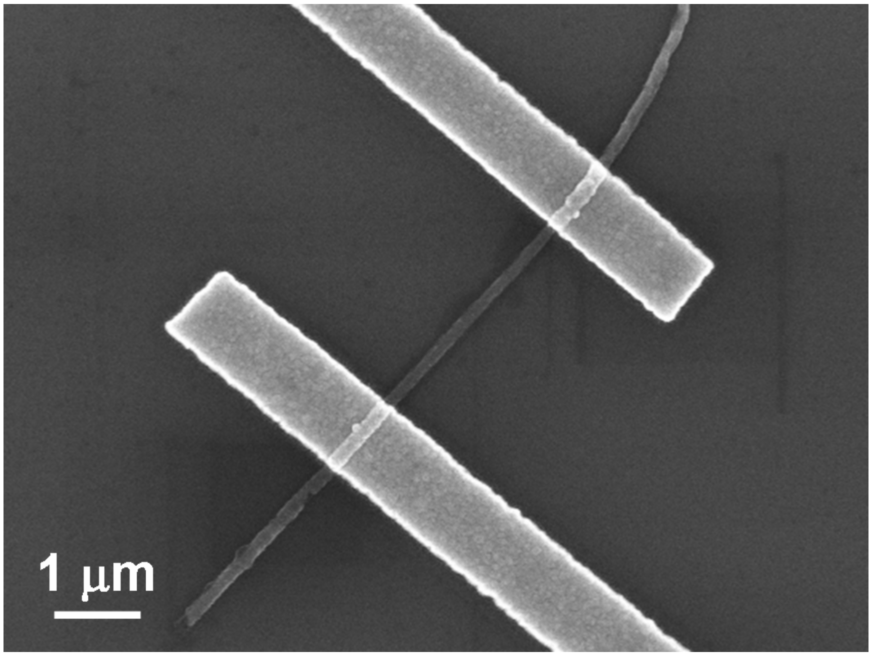

Figure 4.9. SEM of CIS NW-FET device.

In the literature, one can find conflicting reports regarding the effect of concentration of electrolyte on semiconducting nature of CIS electrodeposited films. Few mention that copper rich CIS is p-type and indium rich is n-type,[24,25] but few report p-type for both composition.[26,27] Electrical transport measurements show that the as-synthesized CIS (C-rich and I-rich) NWs are both p-type. The decrease in source-drain current with increase in gate voltage were indicative that both type of NWs are hole conducting (Figures 4.10 and 4.11).

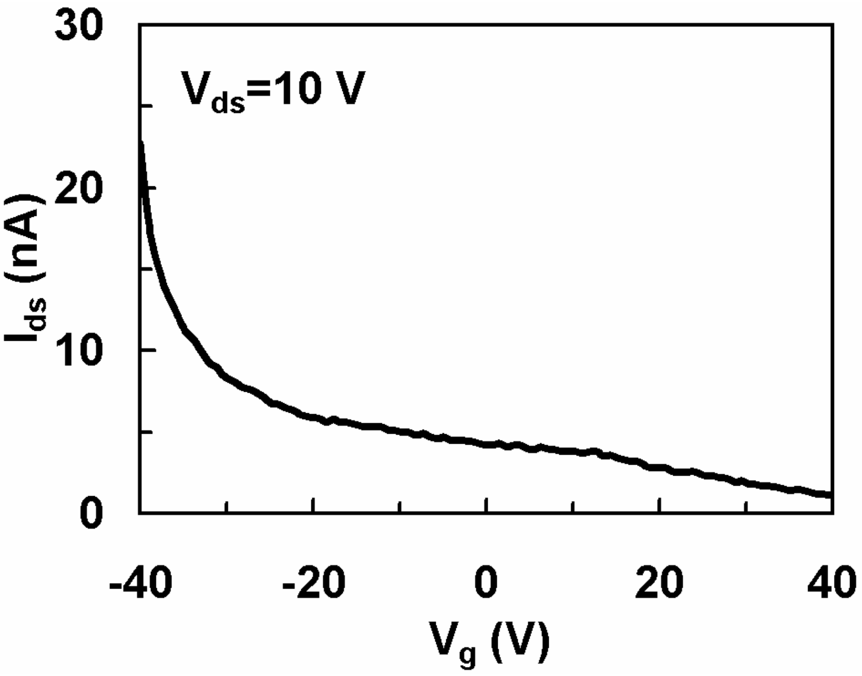

Figure 4.10. I_{ds}-V_g curve of a C-rich NW-FET device.

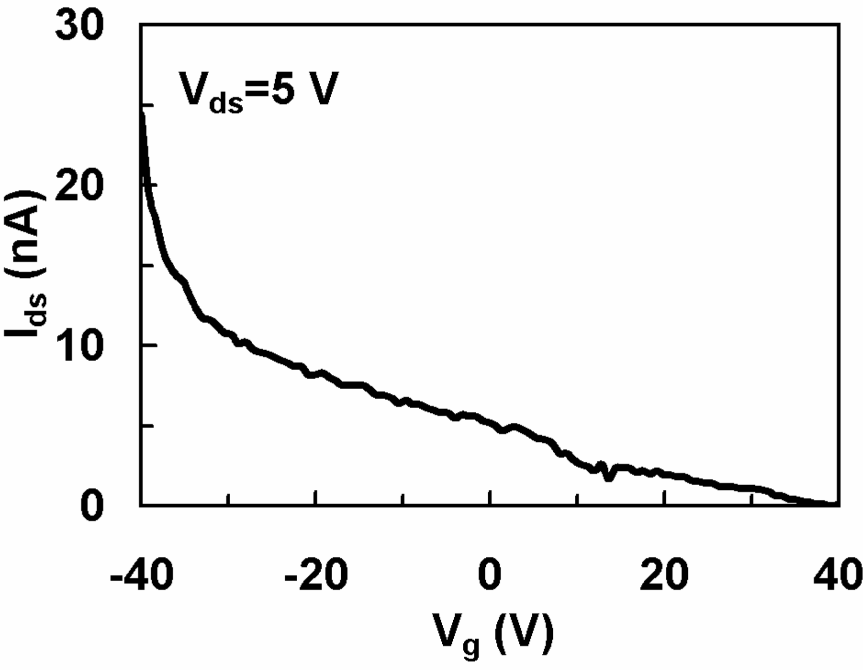

Figure 4.11. I_{ds}-V_g curve of a I-rich NW-FET device.

To further study the potential use of as-synthesized CIS NWs in optoelectronic device applications (i.e. solar cells), their photo sensitivity under the exposure of a 50 W tungsten halogen lamp was investigated. For both samples, the photoconductivity was recorded under an incident photon flux of 50 mW/cm^2 of white light illumination onto the device plane ($\lambda \geq 350$nm) at room temperature and ambient conditions. Figures 4.12 and 4.13 compare the *I-V* characteristics of the CIS NWs under dark and visible light illumination. It can be observed that both devices show high resistivity (above 400 MΩ) in the dark. Furthermore, figure 4.12 shows that no photoresponse was observed for the C-rich device and the *I-V* curves are essentially identical for both illuminating conditions (dark and light illumination).

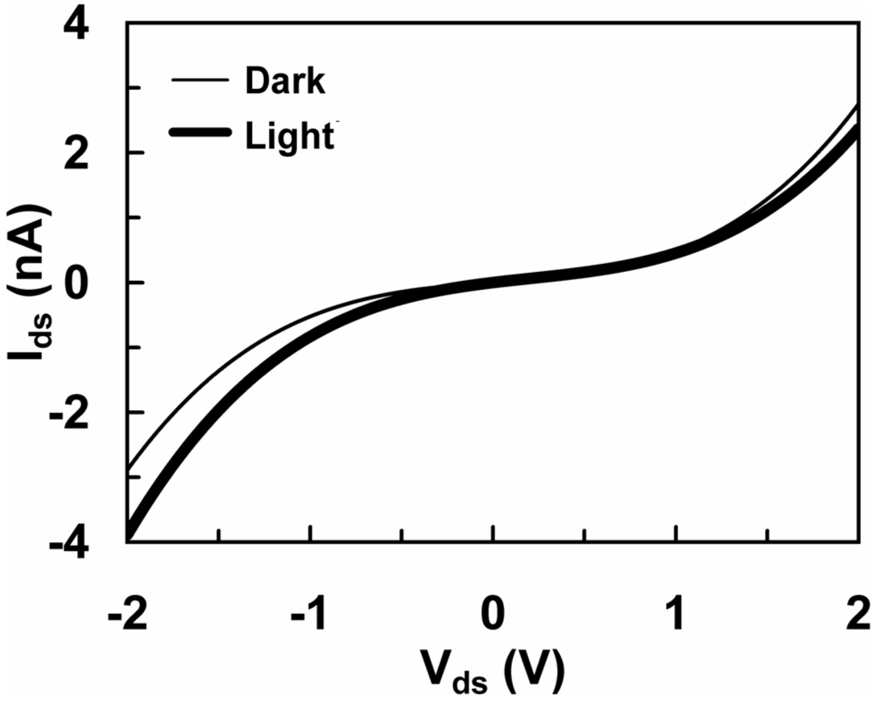

Figure 4.12. *I-V* characteristics of single as-synthesized C-rich NW under dark (thin curve) and under light (thick curve).conditions.

On the other hand, a significant increase was observed in the photoresponse of the I-rich sample when the device was exposed to the halogen light. When the I-rich NWs are exposed to light, the nanowire resistivity decreases by at least more than 1 order of magnitude. For the particular nanowire device sampled in Figure 4.13, the ratio of resistance in dark (R_D) to resistance under light (R_L) is around 10 ($R_D / R_L = 10$). A larger photoresponse is observed at higher bias and the device exhibits nonlinear characteristics during the I-V characterization. The obtained *I-V* characteristics are in agreement with the literature where an decrease in the [Cu]/[In] leads to a increase in the photosensitivity of CIS and the I-rich sample exhibits a significant modulation in the conductance. This leads to a very interesting observation that C-rich NWs are not photoconductive while the In-Rich NWs are.

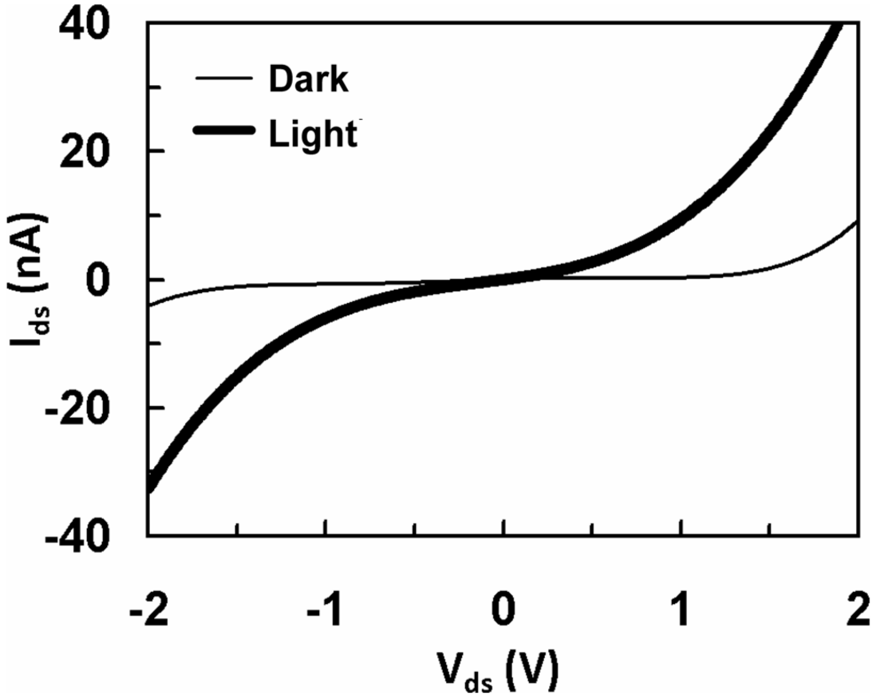

Figure 4.13. *I-V* characteristics of single as-synthesized I-rich NW under dark (thin curve) and under light (thick curve).conditions.

Additionally, *I-V* measurements were conducted on the C-rich and I-rich NWs by CAFM. In a typical experimental setup the electrical measurements were taken transversally across the CIS NWs by applying a potential bias from -5V to 5V. The apex of a conductive Pt/Ir AFM tip (radius of curvature ~25 nm) was used as the top electrode, while a Si/Au substrate was used as the bottom electrode with a single standing NW sandwiched in between both contacts (Fig. 4.14). The *I-V* measurements were taken on different NWs along the same sample as shown in Figure 4.14 and for each NW a set of five measurements were averaged.

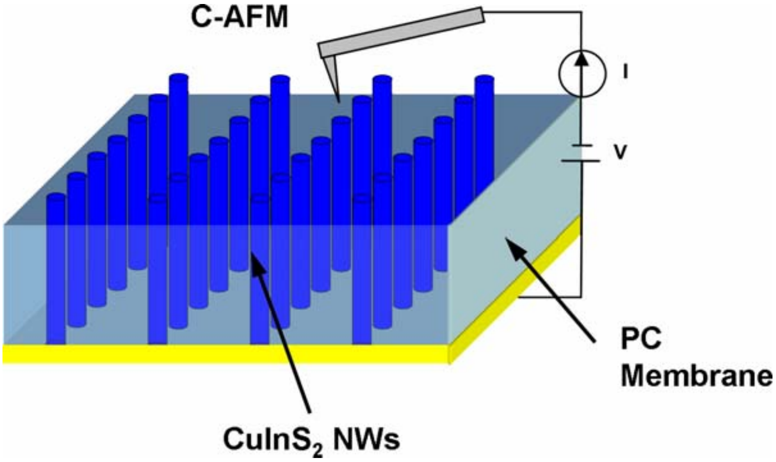

Figure 4.14. Conductive-AFM schematic of as-synthesized NWs embedded in a PC template

Figure 4.15. SEM of as-synthesized NWs embedded in a PC template.

Typical *I-V* curves for the C-rich and I-rich NWs showed a nonlinear and asymmetric behavior; consistent with the metal-semiconductor (M/SC) interface (Schottky contact) formed between the metal electnanostructurees and the semiconducting NWs. Taking into account the high work function of Pt (5.64 eV) that forms a direct contact with the nanostructure allows for the plausible explanation of the observed electrical characteristics of these NWs in terms of a Schottky contact and can be described by the well know Schottky diode theory (neglecting series and shunt resistance),

$$I = I_s \exp\left(\frac{qV}{\eta k_B T} - 1 \right), \qquad (1)$$

Where I_S is the reverse bias saturation current density, k_B is the Boltzmann's constant, T is the absolute temperature and η is the ideality factor (close to unity in conventional Schottky diodes where thermionic emission is dominant). From the slope of ln(I) vs V plot in the $0.1 < V < 1$V linear range the ideality factor η was estimated to be ~9 and 7 for the C-rich and I-rich NWs, respectively. This large deviation from the ideality factor of unity is suggestive that the *I-V* characteristics observed in both NWs are different from the conventional Schottky diode behavior.

As shown in figure 4.16, the I-V characteristic curve for the C-rich sample shows a turn-on voltage of ~0.5V for the forward bias and a reverse bias breakdown voltage of ~-2.5V. On the other hand, it also shows a forward bias a turn-on voltage of ~0.5-1V, while a lower breakdown voltage (compared to the one obtained for C-rich nanostructure) of ~1.5V is observed in the reverse bias of the I-rich sample.

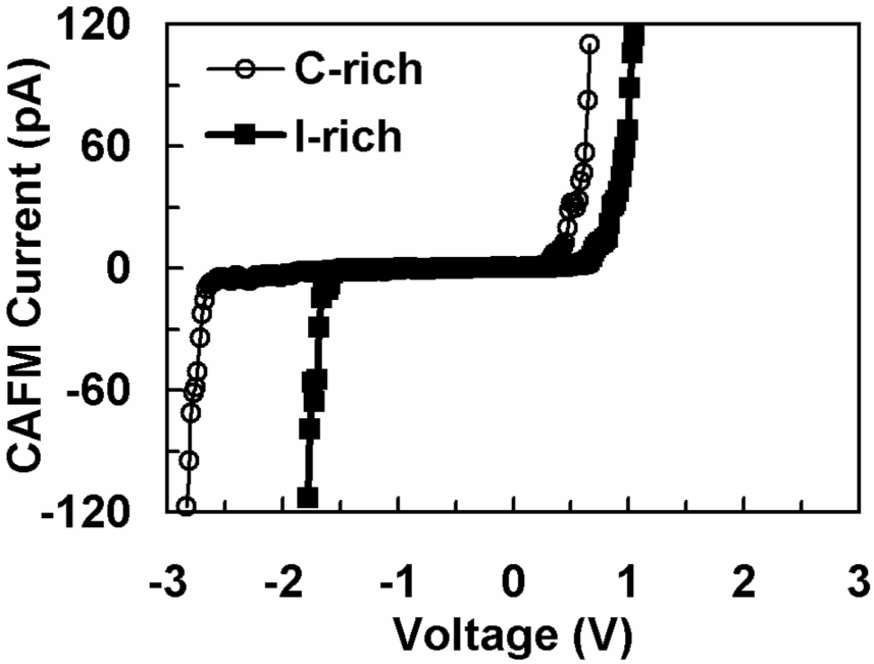

Figure 4.16. Conductive-AFM *I-V* characteristics of single as-synthesized C-rich and I-rich NWs anchored to a thin conductive film.

In this work, we hypothesize that the low breakdown voltage observed for both samples is due to the poor point contact achieved by the conductive AFM tip on the bare CIS nanostructures, leading to an easy breakdown at a low reverse voltage in both cases.

This marked difference observed in electrical and optical properties of CIS NWs indicates the importance of the chemical composition, size and energy level bands of the as synthesized nanostructures and can be related to the partial ion precursor concentrations of different salts in the electrolyte during the synthesis process.

4.5 Discussion

To conclude CIS NWs, with varying chemical composition were synthesized by sonoelectrochemical deposition. This is the first report on the synthesis of CIS NWs by template-assisted electrochemical deposition. The effect of electrolyte composition on electnanostructureeposited NWs was also observed and analyzed. Though structural and spatial properties of Copper rich and Indium rich were similar, there was a remarkable difference in their absorbance and photoconductivity. This marked difference observed in electrical and optical properties of CIS NWs indicates the importance of relative concentration of different salts in the electrolyte. Hence, this template assisted sonoelectrochemical deposition gives us a facile way to tailor the opto-electrical properties of CIS NWs according to device requirements.

4.6 References

1. H. W. Schock, MRS Bulletin 18, 42 (1993)

2. M. C. Lux-Steiner, A. Ennaoui, C. H. Fischer, A. Jager-Waldau, J. Klaer, R. Klenk, R. Konenkamp, T. Matthes, R. Scheer, S. Siebentritt and A. Weidinger, Thin Solid Films 361, 533 (2000)

3. C. Guillen and J. Herrero, Phys. Status Solidi A 203, 2438 (2006)

4. R. W. Birkmire, Sol. Energy Mater. Sol. 65, 17 (2001)

5. J. T. Jiu, S. Isoda, F. M. Wang and M. Adachi, J. Phys. Chem. 110, 2087 (2006)

6. K. P. Jayadevan and T. Y. Tseng, J. Nanosci. Nanotechno. 5, 1768 (2005)

7. W. U. Huynh, J. J. Dittmer and A. P. Alivisatos, Science 295, 2425 (2002)

8. B. M. Kayes, H. A. Atwater and N. S. Lewis, J. Appl. Phys. 97, 11 (2005)

9. J. P. Xiao, Y. Xie, R. Tang and Y. T. Qian, J. Solid State Chem. 161, 179 (2001)

10. Y. Cui, J. Ren, G. Chen, Y. T. Qian and Y. Xie, Chem. Lett. 30, 236 (2001)

11. K. Wakita, M. Iwai, Y. Miyoshi, H. Fujibuchi and A. Ashida, Compos. Sci. Technol. 65, 765 (2005)

12. S. Gorai and S. Chaudhuri, Mater. Chem. Phys. 94, 434 (2005)

13. X. L. Gou, F. Y. Cheng, Y. H. Shi, L. Zhang, S. J. Peng, J. Chen and P. W. Shen, J. Am. Chem. Soc. 128, 7222 (2006)

14. K.V. Singh, A.A. Martinez-Morales, Senthil Andavan G.T., K.N. Bozhilov and M. Ozkan, Chem. Mater. 19, 2446 (2007)

15. M. Krunks, V. Mikli, O. Bijakina, H. Rebane, A. Mere, T. Varema and E. Mellikov, Thin Solid Films 361, 61 (2000)

16. Y. Shi, Z. G. Jin, C. Y. Li, H. S. An, and J. J. Qiu, Appl. Surf. Sci. 252, 3737 (2006)

17. K. S. Suslick, D. A. Hammerton and R. E. Cline, J. Am. Chem. Soc. 108, 5641 (1986)

18. L. Vradman, M. V. Landau, M. Herskowitz, V. Ezersky, M. Talianker, S. Nikitenko, Y. Koltypin, and A. Gedanken, Nanotechnology in Mesostructured Materials 146, 721 (2003)

19. M. L. Tian, J. U. Wang, J. Kurtz, T. E. Mallouk and M. H. W. Chan, Nano Lett. 3, 919 (2003)

20. W. U. Wang, C. Chen, K. H. Lin, Y. Fang and C. M. Lieber, Proc. Nat. Acad. Sci. U.S.A. 102, 3208 (2005)

21. R. Karnik, R. Fan, M. Yue, D. Y. Li, P. D. Yang and A. Majumdar, Nano Lett. 5, 943 (2005)

22. D. J. Sirbuly, M. Law, H. Q. Yan and P. D. Yang, J. Phys. Chem. B 109, 15190 (2005)

23. C. B. Mao, D. J. Solis, B. D. Reiss, S. T. Kottmann, R. Y. Sweeney, A. Hayhurst, G. Georgiou, B. Iverson and A. M. Belcher, Science 303, 213 (2004)

24. G. Hodes, T. Engelhard, D. Cahen, L. L. Kazmerski and C. R. Herrington, Thin Solid Films 128, 93 (1985)

25. G. Hodes, T. Engelhard, C.R. Herrington, L.L. Kazmerski and D. Cahen. Prog. Cryst. Growth Charact. Mater. 10, 241 (1984)

26. T. Yukawa, K. Kuwabara and K. Koumoto, Thin Solid Films 286, 151 (1996)

27. A. M. Martinez, L. G. Arriaga, A. M. Fernandez and U. Cano, Mater. Chem. Phys. 88, 417 (2004)

Chapter 5. Electrical Characterization of Composition Modulated $In_{1-x}Sb_x$ Nanowire Field Effect Transistors by SGM

5.1 Introduction

In recent years, there has been an increasing interest in the research of non-silicon electronic materials such as carbon nanotubes,[1] graphene,[2] Ge,[3] and III-V semiconductor compound materials. Specifically, In-based III-V material systems such as InP,[4] InAs,[5] and InSb[6] have been extensively used for decades in communication and optoelectronic applications and are considered to be mature technologies.

Among the In-V semiconductors compounds, InSb stands out as an attractive candidate for the realization of low power and ultra-high speed logic applications. The remarkable intrinsic properties of InSb at room temperature, such as high electron mobility ($\sim 7.8 \times 10^4$ cm^2 V^{-1}s^{-1}), direct low band gap (0.18 eV) and long ballistic mean-free path (0.58 μm)[7] are of great interest to researchers and industry. As a case in point of the growing interest in InSb, Intel and QinetiQ have already demonstrated the implementation of high performance enhancement and depletion-mode InSb quantum well (QW) transistors fabricated on semi-insulating GaAs substrates.[8]

InSb NWs have been synthesized using various methods such as epitaxial growth,[9] MOCVD,[10] CVD,[11] direct antimonidization of In droplets[12] and electrodeposition in a porous template[13]. Although several reports on the synthesis of InSb thin films and NWs have been reported in the literature, the intrinsic electrical characteristics of these NWs have been studied in a much less degree.

Particularly, few systematic studies have been reported on the effects of In and Sb concentration and the role each element plays in the optical and electrical characteristics of the alloy.[14,15] One-dimensional $In_{1-x}Sb_x$ NWs, in this sense, can serve as attractive test beds to investigate the relationship between composition modulation and electronic charge transport characteristics.

This type of study is of great interest in the area of nanoelectronics since as it has already been demonstrated that it is possible to integrate optical and electrical components within individual NWs.[16,17]

To this end, we report the synthesis and characterization of *n*-type and *p*-type $In_{1-x}Sb_x$ NWs for their potential use as elemental device blocks in electronic applications. Using a scanning gate microscopy (SGM) method we characterized the electrical transport characteristics of composition modulated $In_{1-x}Sb_x$ nanowire field effect transistor (NW-FET) devices. A conductive AFM probe was used as a local gate electrode[18] to induce a local change of the electron (or hole) density as a method to modulate the current transport through the fabricated NW-FET devices. Because of the small channel width (~100nm) of the NW-FETs the sensitivity to local gating can be expected to be significantly large as a small gated region of the NWs can effectively limit the total conductance.[19]

5.2 Materials and Methods

5.2.1 Synthesis of Composition Modulated $In_{1-x}Sb_x$ (x~0.5 or 0.7) Nanowires

The $In_{1-x}Sb_x$ NWs used in this work were prepared by an electrochemical deposition method. A detailed description of the synthesis process and complete characterization of the crystalline nature of InSb NWs grown via this method has been reported by our group elsewhere.[20] In short, sono assited-electrodeposition was performed in a typical three-electrode electrochemical cell setup with a platinum electrode as the counter electrode and a Ag/AgCl electrode as the reference electrode. A gold-coated template was used as the working electrode during deposition and controlled by a Potentiostat/Galvanostat instrument. The electrolyte partial concentrations were optimized as follows: 100 mM $SbCl_3$, 150 mM $InCl_3$, 360 mM citric acid and 170 mM potassium citrate at a pH of 1.8. The citrate ions are used as the complexing agents to bring the deposition potential of In and Sb closer to maintain binary growth.

In this specific study, a polycarbonate (PC) membrane was used instead of the commonly used Al_2O_3 as the growth template. This was done based on the fact that the etching process of the polycarbonate matrix in chloroform, has no adverse effects on the integrity of the InSb NWs (i.e. structural damage) compared to NaOH used to dissolve Al_2O_3. A comprehensive account of the experimental details on the electrodeposition of composition modulated InSb NWs will be reported in a separate publication. In short, using a single bath method $In_{0.5}Sb_{0.5}$ and $In_{0.3}Sb_{0.7}$ NWs were attained by selectively applying a deposition potential during growth of -0.6V or -1.8V, respectively.

5.3 Characterization of Composition Modulated $In_{1-x}Sb_x$ (x~0.5 or 0.7) Nanowires

5.3.1 SEM characterization

Figure 5.1 shows an SEM image of a randomly oriented matrix of standing $In_{1-x}Sb_x$ NWs. After the PC membrane has been completely dissolved, the NWs resemble a grass-like structure as they remained anchored to the growth substrate. Figure 5.2 shows that the as-grown NWs are about 100 nm in diameter with typical lengths of 6-8μm. Additionally, the morphology of the NWs appear to be of high-quality with the overall sample free of any residue or contaminants derived from the synthesis process.

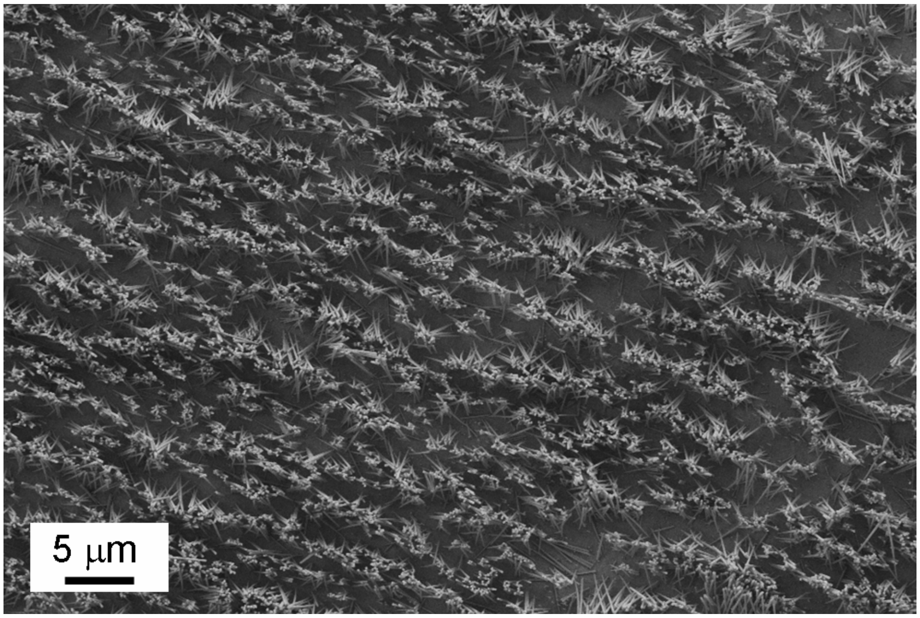

Figure 5.1. Low resolution SEM image of as-grown $In_{1-x}Sb_x$ NWs standing on Au thin film.

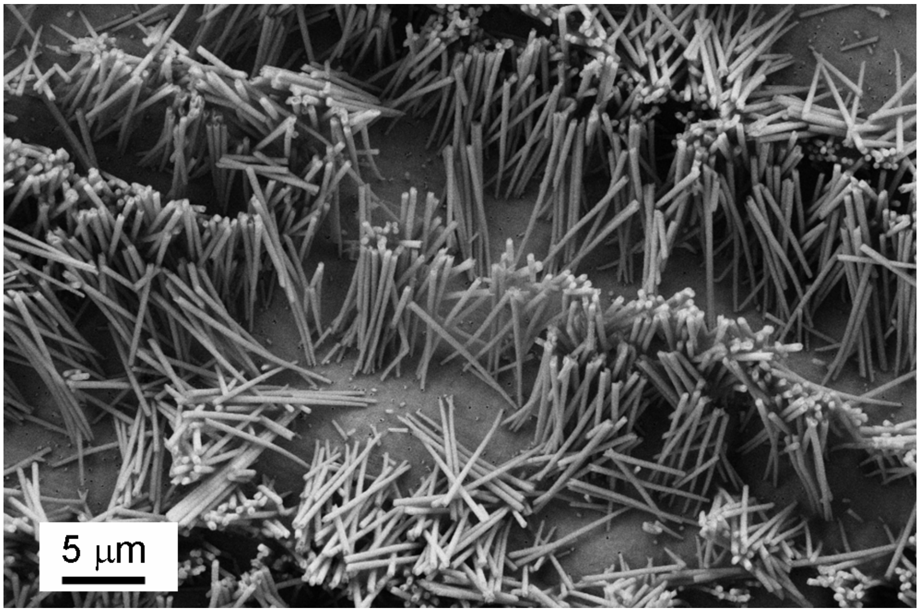

Figure 5.2. Higher resolution SEM of the structural quality of as-grown NWs.

Figures 5.3 and 5.4 show typical SEM images of as-grown composition modulated $In_{0.5}Sb_{0.5}$ and $In_{0.3}Sb_{0.7}$ NW bundles respectively. The images were taken after the as-grown NWs were freed from the conductive thin film by a gentle sonication.

5.3.2 Composition Characterization by EDS

The relative composition of In and Sb in the electrodeposited $In_{1-x}Sb_x$ NWs was determined from energy dispersive x-ray (EDX) measurements probed on individual NWs. Using the measured radiations from the EDX spectra we quantitatively determined the relative In and Sb composition as representatively shown for $In_{0.5}Sb_{0.5}$ and $In_{0.3}Sb_{0.7}$ NWs in figures 5.5 and 5.6, respectively.

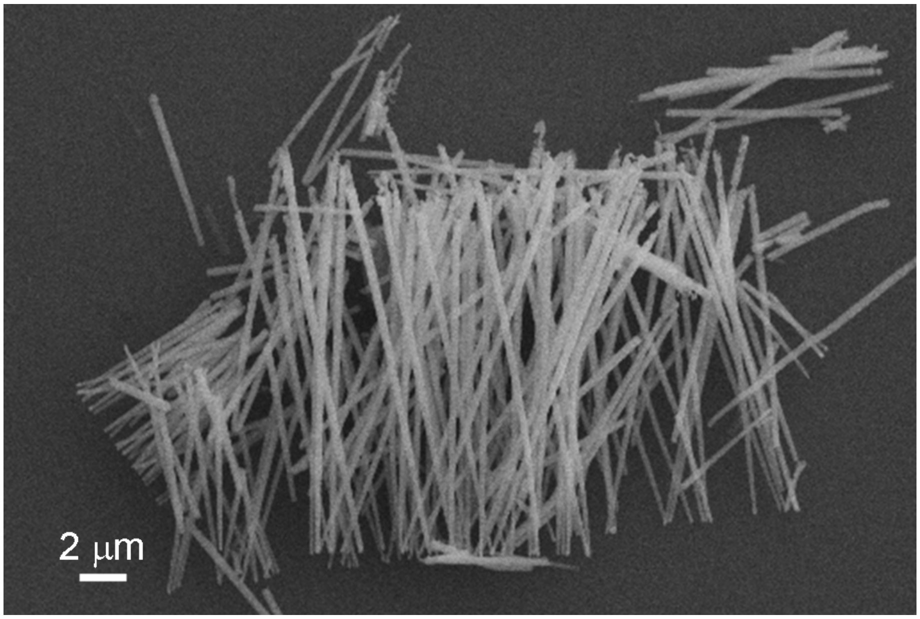

Figure 5.3. SEM image of a representative bundle of as-grown $In_{0.5}Sb_{0.5}$ NWs.

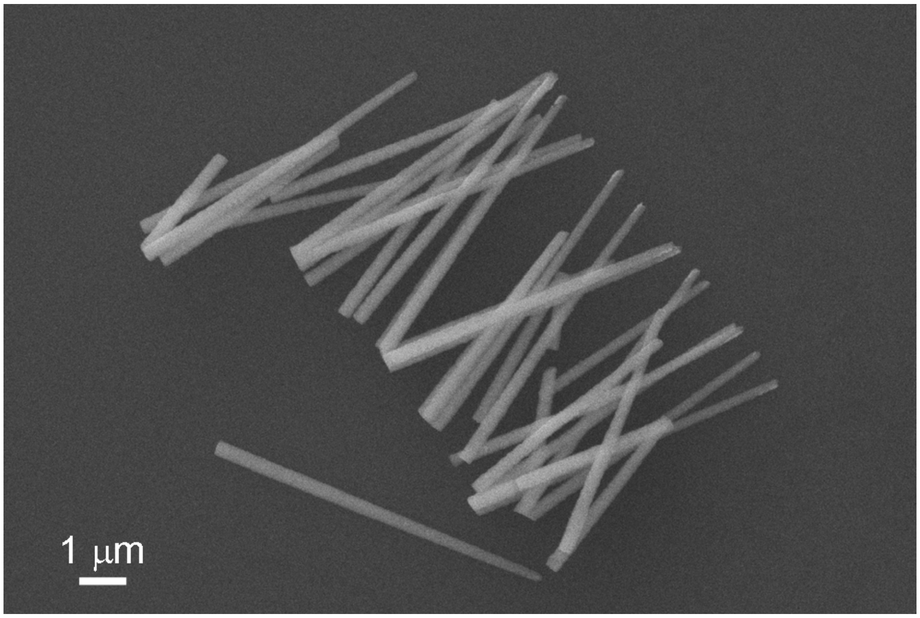

Figure 5.4. SEM image of a representative bundle of as-grown $In_{0.3}Sb_{0.7,}$ NWs.

In both cases the EDX spectrum shows that the as-grown NWs consist of In and Sb in an atomic ratio of approximately 1:1 and 3:7 and the In:Sb composition along individual NWs is variant only within 5% variation. This finding suggests that appropriate alloying of In and Sb within the NWs has been achieved without forming any obvious disorder in the structure or stoichiometric composition. The EDX results were reproducible over the entire growth substrate, demonstrating that this technique is capable of producing $In_{1-X}Sb_X$ NWs with uniform and well controlled compositions over large areas.

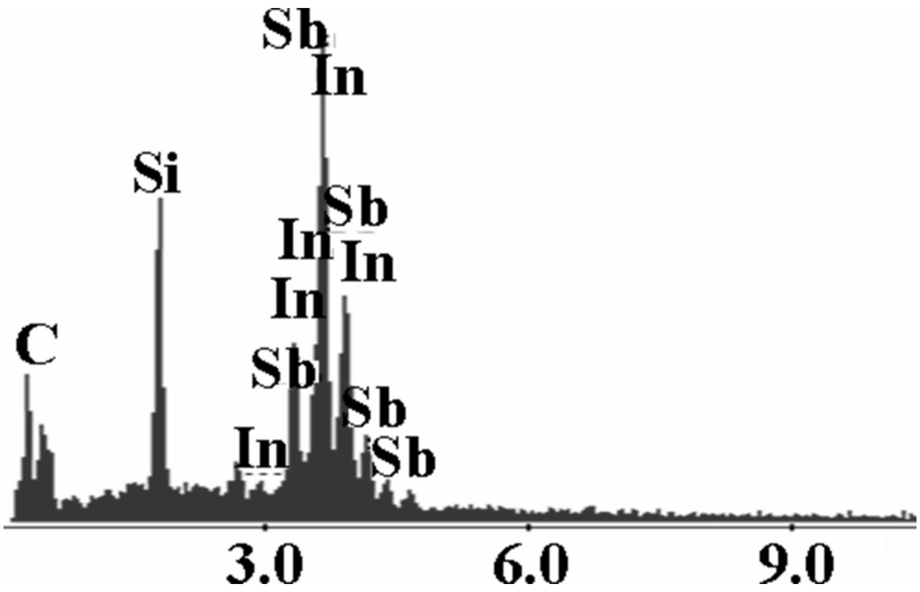

Figure 5.5. EDS spectrum taken from a bundle of as-grown $In_{0.5}Sb_{0.5}$.NWs.

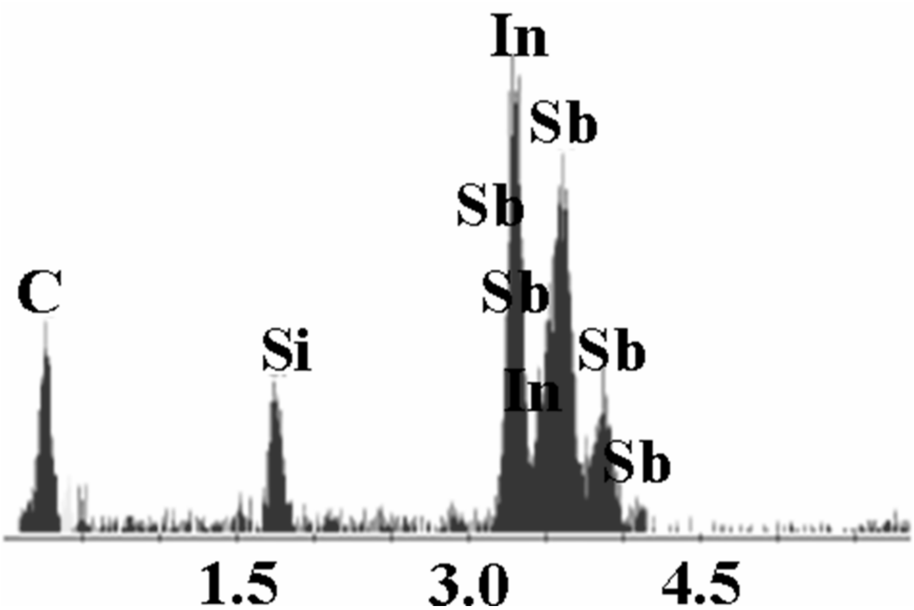

Figure 5.6. EDS spectrum taken from a bundle of as-grown $In_{0.3}Sb_{0.7}$.NWs.

5.3.3 Electrical Characterization by SGM

Using the as-grown $In_{1-x}Sb_x$ NWs, *n*-type and *p*-type NW-FETs were fabricated on n-Si/SiO_2 (50nm) substrate by using electron-beam lithography (EBL) to define the source and drain contacts.Electron-beam evaporation was used to deposit Ti/Au (10nm/90nm) contact electrodes. Atomic layer deposition (ALD) was used to deposit a 20nm layer of Al_2O_3 as the gate dielectric. Using a Pt/Ir coated AFM probe, as a top local gate electrode, a gate voltage (V_g) was applied under a constant force feedback mechanism during SGM measurements.

5.4 Results

In order to estimate and compare the resistivity of as-grown $In_{0.5}Sb_{0.5}$ and $In_{0.3}Sb_{0.7}$ NWs, we conducted two terminal current-voltage (*I-V*) measurements. The resistance for the composition modulated $In_{1-x}Sb_x$ (x~0.5 and 0.7) NWs was calculated by using a differential voltage method on the linear portion of the *I-V* curves shown in figures 5.7 and 5.8. A resistance of about 46.6 x 10^3 Ω and 4.7 x 10^6 Ω were calculated for the $In_{0.5}Sb_{0.5}$ and $In_{0.3}Sb_{0.7}$ NWs, respectively. The observed linearity at a low voltage bias, in the central region of the *I-V* curves, originate from a low-resistance ohmic contact characteristic of a InSb-metal interface,[21] resulting from the occurrence of a surface Fermi level pinning.[22]

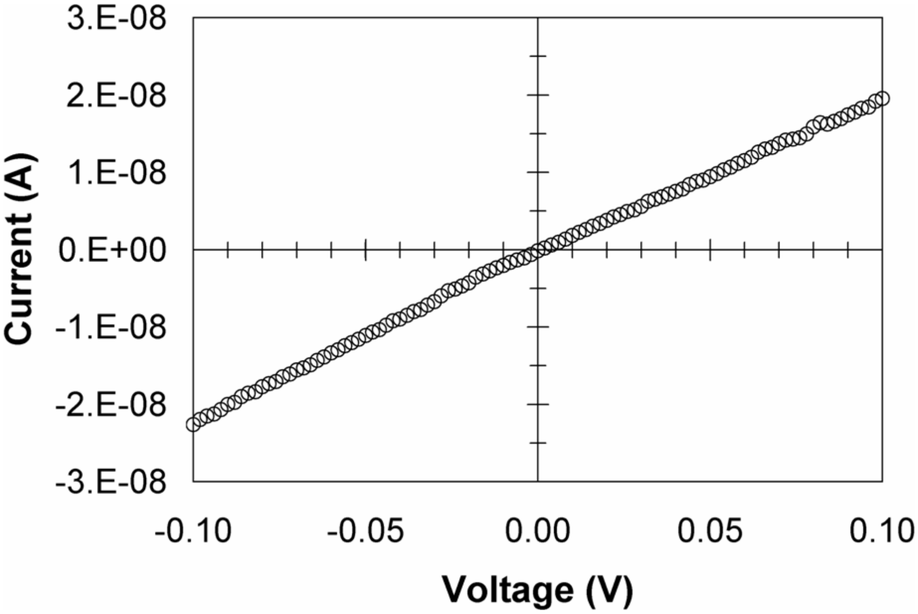

Figure 5.7. *I-V* electrical characteristics of an $In_{0.5}Sb_{0.5}$ NW.

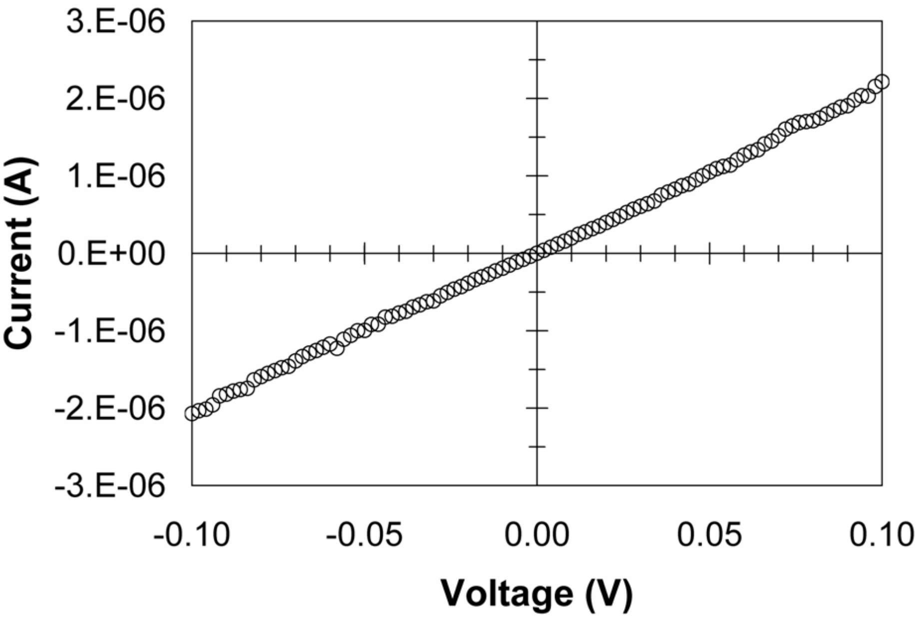

Figure 5.8. *I-V* electrical characteristics of an $In_{0.3}Sb_{0.7}$ NW.

Furthermore, taking into account the physical dimensions of the NWs in both measurements (a length of 2 μm and radius of 100 nm), we calculated the resistivity (ρ) of the composition modulated NWs to be about 18.3 mΩ-cm for the $In_{0.5}Sb_{0.5}$ and 1.8 Ω-cm for the $In_{0.3}Sb_{0.7}$ NWs . The observed increase in resistivity in the $In_{0.3}Sb_{0.7}$ NWs can be understood in terms of a much lower mobility of charge carriers induced by the greater concentration of impurities present in the NWs with the excess antimony.[23]

Figures 5.9 and 5.10 show the schematic for the SGM characterization setup and a contact mode AFM image of a single InSb NW-FET device. The device in figure 5.10 was fabricated using a $In_{0.3}Sb_{0.7}$ NW with a length between the source and drain of about 6.5 μm.

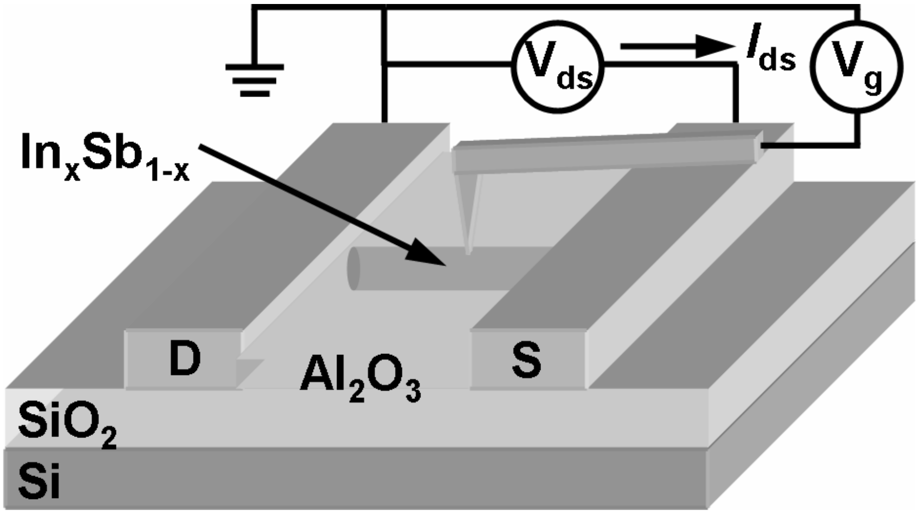

Figure 5.9. Schematic of the SGM setup for characterization of $In_{1-x}Sb_x$ NWFET.

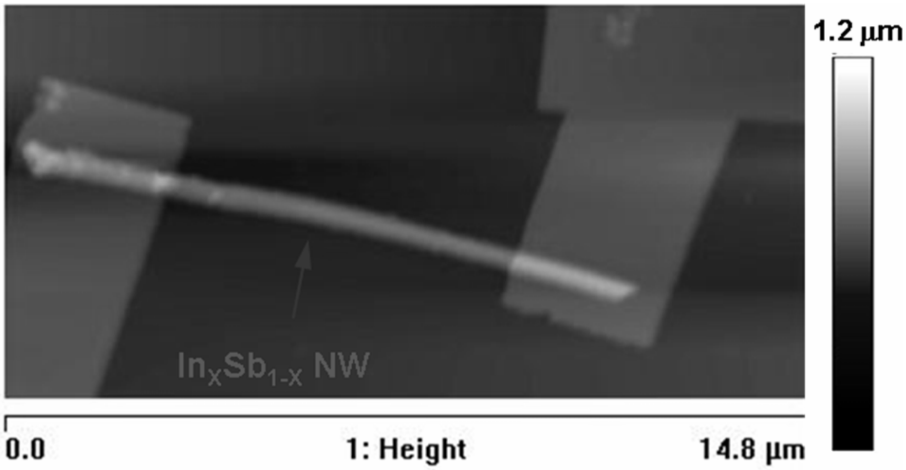

Figure 5.10. AFM height image of an $In_{1-x}Sb_x$ NW FET device characterized in this study.

Figures 4 (c) and (d) show the I_{ds}-V_{ds} characteristics of *n*-type ($In_{0.5}Sb_{0.5}$) and *p*-type ($In_{0.3}Sb_{0.7}$) NW-FET devices at various V_g tested in this study. From both figures, it can be observed that when a gate voltage is locally applied to the middle of the NW-FET using a conductive AFM probe, the I-V characteristics exhibit a significant current modulation. In the case of the $In_{0.5}Sb_{0.5}$ NW-FET device, when the V_g is biased from 0V to 9V, it can be seen that the conductance through the device channel is effectively enhanced for increasingly positive V_g. In contrast, the $In_{0.3}Sb_{0.7}$ NW-FET shows an increase in conductance as a negative V_g is applied to the device. Furthermore, both type of devices show typical depletion mode (normally on) transistor behavior. Using the I_{ds}-V_g curves measured at V_{ds} = 1V for both devices, we were able to confirm the n-type and p-type semiconductor behavior of each fabricated device. From the linear region of I_{ds}-V_g, a normalized transconductance (g_m/W) was extrapolated to be ~4.1 μS/μm for the $In_{0.5}Sb_{0.5}$ NW-FET and ~0.4 mS/μm for the $In_{0.3}Sb_{0.7}$ NW-FET device.

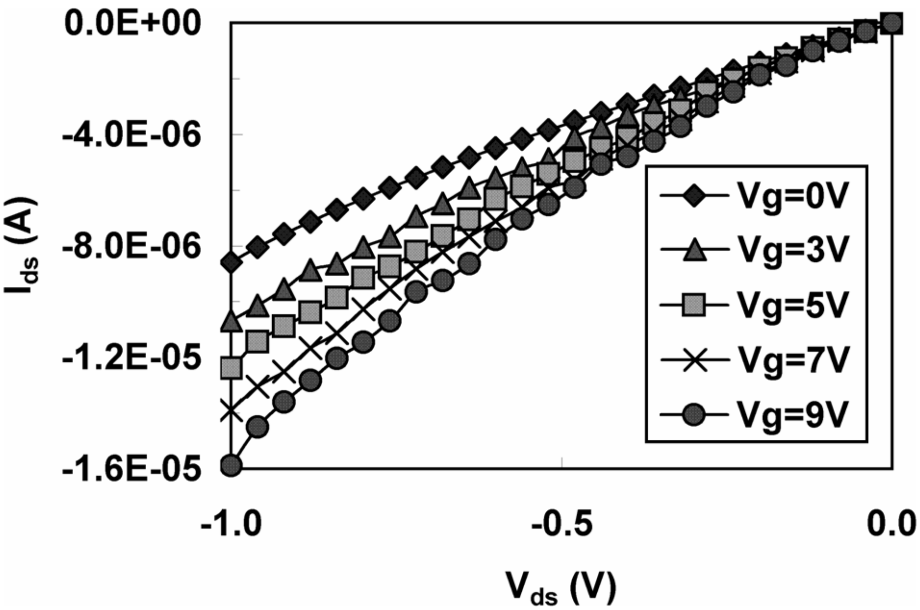

Figure 5.11. I_{ds}-V_{ds} characteristic curves as a function of V_g for $In_{0.5}Sb_{0.5}$ NW-FET device.

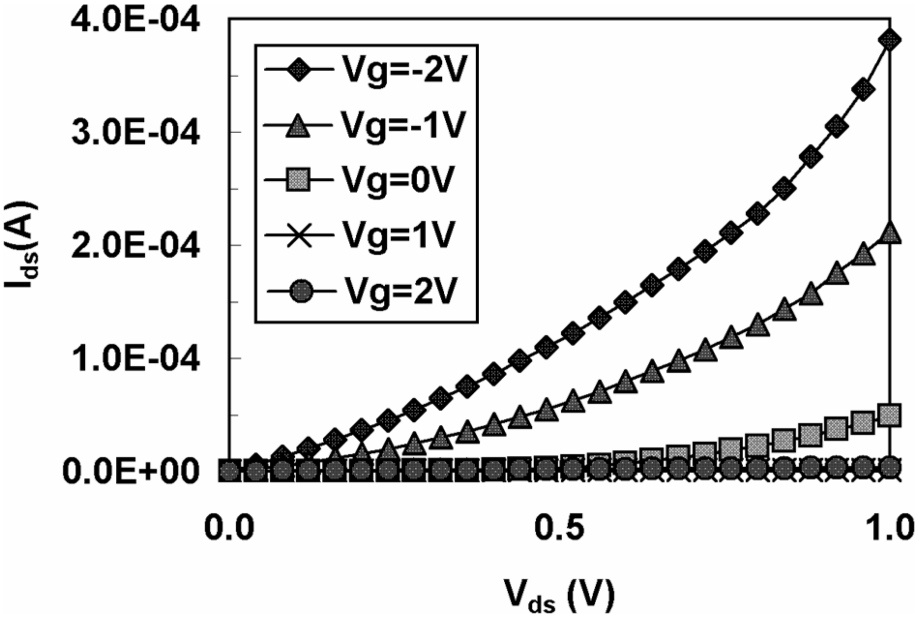

Figure 5.12. I_{ds}-V_{ds} characteristic curves as a function of V_g for $In_{0.3}Sb_{0.7}$ NW-FET device.

5.5 Discussion

The observed conductance modulation can be explained in terms of a tip-induced local energy band bending.[24] Since the conductive AFM probe has a radius of curvature of ~30nm, its localized electrostatic potential has a pronounced effect on the electronic structures on the composition modulated $In_{1-x}Sb_x$ NWs. It is known that band structure modulation by a local electrostatic potential could significantly alter the transport characteristics of quasi one-dimensional nanosystems.[18,25] By using SGM as a characterization technique in this study we have been able to demonstrate FET operation based on *n*-type and *p*-type composition modulated $In_{1-x}Sb_x$ NWs.

5.6 References

1. R. H. Baughman, A. A. Zakhidov, and W. A. de Heer, Science **297**, 787 (2002).

2. A. K. Geim and K. S. Novoselov, Nat. Mater. **6**, 183 (2007).

3. A. B. Greytak, L. J. Lauhon, M. S. Gudiksen, and C. M. Lieber, Appl. Phys. Lett. **84**, 4176 (2004).

4. M. Mokhtari, T. Swahn, R. H. Walden, W. E. Stanchina, M. Kardos, T. Juhola, G. Schuppener, H. Tenhunen, and T. Lewin, IEEE J Solid-State Circuits **32**, 1371 (1997).

5. J. Y. Marzin, J. M. Gérard, A. Izraël, D. Barrier, and G. Bastard, Phys. Rev. Lett. **73**, 716 (1994).

6. A. G. Foyt, W. T. Lindley, and J. P. Donnelly, Appl. Phys. Lett. **16**, 335 (1970).

7. T. Ashley, A. B. Dean, C. T. Elliott, R. Jefferies, F. Khaleque, and T. J. Phillips, in Int. Electron Devices Meeting, 1997, IEDM Technical Digest IEEE International, p. 751.

8. S. Datta, T. Ashley, J. Brask, L. Buckle, M. Doczy, M. Emeny, D. Hayes, K. Hilton, R. Jefferies, T. Martin, T. J. Phillips, D. Wallis, P. Wilding, and R. Chau, in Electron Devices Meeting, 2005, IEDM Technical Digest IEEE International, 2005, p. 763.

9. H. D. Park, S. M. Prokes, M. E. Twigg, Y. Ding, and Z. L. Wang, J. Cryst. Growth **304**, 399 (2007).

10. R. M. Biefeld, Mater. Sci. Eng., R **36**, 105 (2002).

11. J. H. Seol, A. L. Moore, S. K. Saha, F. Zhou, L. Shi, Q. L. Ye, R. Scheffler, N. Mingo, and T. Yamada, J. Appl. Phys. **101**, 023706 (2007).

12. S. Vaddiraju, M. K. Sunkara, A. H. Chin, C. Z. Ning, G. R. Dholakia, and M. Meyyappan, J. Phys. Chem. C **111**, 7339 (2007).

13. X. Zhang, Y. Hao, G. Meng, and L. Zhang, J. Electrochem. Soc. **152**, C664 (2005).

14. L. Chou, Thin Solid Films **215**, 188 (1992).

15. K. Lu, Q. Wang, C. Li, Y. Wang, and X. Chen, J. Non-Cryst. Solids **312-314**, 34 (2002).

16. Y. Li, F. Qian, J. Xiang, and C. M. Lieber, Mater. Today **9**, 18 (2006).

17. O. Hayden, R. Agarwal, and C. M. Lieber, Nat. Mater. **5**, 352 (2006).

18. X. Zhou, S. A. Dayeh, D. Wang, and E. T. Yu, Appl. Phys. Lett. **90**, 233118 (2007).

19. N. R. Wilson and D. H. Cobden, Nano Lett. **8**, 2161 (2008).

20. M. I. Khan, W. Xu, N. B. Krassimir, and S. O. Cengiz, J. Nanomater. **2008**, 1 (2008).

21.C. A. Mead and W. G. Spitzer, Physical Review **134**, A713 (1964).

22. R. J. Egan, V. W. L. Chin, and T. L. Tansley, Semicond. Sci. Technol., 1591 (1994).

23. H. Okimura, Y. Koizumi, and S. Kaida, Thin Solid Films **254**, 169 (1995).

24. M. Morgenstern, in *Scanning Probe Microscopy* (Springer New York, New York, 2007), p. 349.

25. M. Freitag, M. Radosavljevic, Y. Zhou, A. T. Johnson, and W. F. Smith, Appl. Phys. Lett. **79**, 3326 (2001).

Chapter 6. Conclusion

6.1 CPMV-QD(1.2) Hybrid System as a Bistable Memory Element

Although the nanoparticle toolset applied in this work can be considered rather exotic, the resilience and monodispersity of CPMV, combined with unique electronic properties of surface passivated QDs, comprise a relevant material selection for hybrid nanoelectronic devices. Multi-site patterning of two unique QDs was driven by a bio-template on substrate approach, enhancing previous solution based bioconjugation. If the individual interconnect problems is addressed, based on observed electrical characterization, a single CPMV-QD(1,2) hybrid of 40nm showing reversible bistable behavior shows promise for future digital memory applications.

6.2 CPMV-IO Hybrid as an Scaffold System to Enhanced the Local Magnetic Field Strength of IO Nanoparticles

The enhanced local magnetic field strength was qualitatively analyzed by MFM, demonstrating a characteristic advantage for attaching derivatized magnetic IO nanoparticles in an organic medium. During MFM characterization a ‘boundary-effect’ was observed at the CPMV/IO interface. A strong magnetic field gradient was measured by the probe and the cantilever experienced a strong attractive force during MFM measurements. This strong interaction at a lift-off distance of 65 nm was indicative of a strong local magnetic field most likely due to a cumulative dipole effect of several IO nanoparticles clustered together. Such assembly processes are desirable in tailoring the physical-magnetic properties of a mutant hybrid which could provide multifunctional nanoparticles for enhanced MRI imaging.

6.3 $CuInS_2$ Nanowires as a Photosensitive Material

CIS NWs, with varying chemical composition and stoichiometry were synthesized by sonoelectrochemical deposition. This is the first report on the synthesis of CIS NWs by template-assisted sonoelectrochemical deposition. The effect of electrolyte composition on electrodeposited NWs was also observed and analyzed. Though structural and spatial properties of Copper rich and Indium rich were similar, there was a pronounce difference in their photoconductivity. This marked difference observed in electrical and optical properties of CIS NWs indicates the importance of relative concentration of different salts in the electrolyte. Hence, this template assisted sonoelectrochemical deposition gives us a facile way to tailor the opto-electrical properties of CIS NWs according to device requirements.

6.4 Composition Modulated $In_{1-x}Sb_x$ (x~0.5 or 0.7) NWs as Nanowire Field Effect Transistors

In conclusion, we have reported in this work the electrochemical synthesis of crystalline composition modulated $In_{1-x}Sb_x$ NWs. Complementary doping of $In_{1-x}Sb_x$ NWs was achieved by Sb incorporation during the electrodeposition by controlling the deposition potential. Electrical transport measurements showed that the as-grown NWs exhibit *n*-type or *p*-type semiconducting properties depending on the amount of Sb atomic concentration x (in %) present in their composition as determined by the deposition potential used during synthesis. Based on our results we argue that the availability of both *n* and *p*-type $In_{1-x}Sb_x$ NW components suggests the possible application of InSb NWs in electronic and optoelectronic applications. The results presented here intend to help elucidate some basic understanding of the inherent electrical characteristics of composition modulated $In_{1-x}Sb_x$ NWs.